JGR Oceans

RESEARCH ARTICLE

10.1029/2020JC016246

Key Points:

- Turbulent dissipation at mid depth linked to sheared flow generated by eddy-topography interaction
- Elevated dissipation associated with centrifugal instability where eddy flow was blocked by topography
- Dissipation in the lee of an escarpment with internal wave generation and possible hydraulic jump

Correspondence to:

D. G. Evans,
dgwynevans@noc.ac.uk

Citation:

Evans, D. G., Frajka-Williams, E., Naveira Garabato, A. C., Polzin, K. L., & Forryan, A. (2020). Mesoscale eddy dissipation by a "zoo" of submesoscale processes at a western boundary. *Journal of Geophysical Research: Oceans*, *125*, e2020JC016246. https://doi.org/10.1029/2020JC016246

Received 18 MAR 2020
Accepted 2 NOV 2020

© 2020. The Authors.
This is an open access article under the terms of the Creative Commons Attribution License, which permits use, distribution and reproduction in any medium, provided the original work is properly cited.

Mesoscale Eddy Dissipation by a "Zoo" of Submesoscale Processes at a Western Boundary

Dafydd Gwyn Evans[1], Eleanor Frajka-Williams[1], Alberto C. Naveira Garabato[2], Kurt L. Polzin[3], and Alexander Forryan[2]

[1]National Oceanography Centre, Southampton, UK, [2]Ocean and Earth Science, University of Southampton, Southampton, UK, [3]Woods Hole Oceanographic Institution, Woods Hole, MA, USA

Abstract Mesoscale eddies are ubiquitous dynamical features that tend to propagate westward and disappear along ocean western boundaries. Using a multiscale observational study, we assess the extent to which eddies dissipate via a direct cascade of energy at a western boundary. We analyze data from a ship-based microstructure and velocity survey, and an 18-month mooring deployment, to document the dissipation of energy in anticyclonic and cyclonic eddies impinging on the topographic slope east of the Bahamas, in the North Atlantic Ocean. These observations reveal high levels of turbulence where the steep and rough topographic slope modified the intensified northward flow associated with, in particular, anticyclonic eddies. Elevated dissipation was observed both near-bottom and at mid depths (200–800 m). Near-bottom turbulence occurred in the lee of a protruding escarpment, where elevated Froude numbers suggest hydraulic control. Energy was also radiated in the form of upward-propagating internal waves. Elevated dissipation at mid depths occurred in regions of strong vertical shear, where the topographic slope modified the vertical structure of the northward eddy flow. Here, low Richardson numbers and a local change in the isopycnal gradient of potential vorticity (PV) suggest that the elevated dissipation was associated with horizontal shear instability. Elevated mid-depth dissipation was also induced by topographic steering of the flow. This led to large anticyclonic vorticity and negative PV adjacent to the topographic slope, suggesting that centrifugal instability underpinned the local enhancement in dissipation. Our results provide a mechanistic benchmark for the realistic representation of eddy dissipation in ocean models.

1. Introduction

Mesoscale eddies are ubiquitous in the world's oceans. They typically have a diameter of the order 100 km and generally propagate westward, transferring energy and momentum, affecting budgets of heat, salt, and carbon (Chelton et al., 2011), and accounting for over 80% of global oceanic kinetic energy (Ferrari & Wunsch, 2009). Mesoscale eddies are therefore a key part of the global ocean energy budget, yet the pathways of energy to and from the mesoscale are poorly constrained. Energy may be transferred from the mesoscale via a direct cascade to smaller scales, where it is dissipated. Alternatively, mesoscale energy can be transferred onto larger scales via an inverse cascade (Scott & Wang, 2005). Identifying and quantifying these pathways for energy transfer from the mesoscale is a critical step toward the realistic representation of eddy dynamics and their impacts on climatic variability in ocean models.

Satellite observations tell us that mesoscale eddies disappear at the steep and rough topography of the western boundaries of ocean basins (Zhai et al., 2010), suggesting that these regions may acts as eddy dissipation hotspots. The situations under which energy may be transferred to larger or smaller scales remain ambiguous, however. Both are possible and perhaps likely. Through a broad range of potential interactions, when the geostrophically near-balanced mesoscale eddy flows encounter steep topography they may become unstable, generating turbulence that dissipates mesoscale energy. In this way, eddy-topography interactions at western boundaries may play an important role in the dissipation of eddy energy via a direct cascade to small scales. Understanding these eddy-topography interactions is an open problem that has recently spurred a broad range of studies, which we will now briefly review.

Investigations of eddy-topography interactions have ranged from simple reduced-gravity simulations with vertical sidewalls and single eddies (Hogg et al., 2011), to increasingly more complex simulations with

sloping topography, multiple interacting eddies, and continuous stratification (Cherian & Brink, 2016, 2018; Dewar & Hogg, 2010; Dewar et al., 2011; Zhang & Partida, 2018). Several of these studies have some observational basis, using observations to motivate and justify the configuration of a given simulation (Zhang & Gawarkiewicz, 2015; Zhang & Partida, 2018), while others have focused solely on observational data (Clément et al., 2016). The existing analyses also tackle a range of spatial scales, from single vortices (Hogg et al., 2011) to entire basins (Zhai et al., 2010).

Using a series of simulations and numerical arguments, Dewar and Hogg (2010), Dewar et al. (2011), and Hogg et al. (2011) show that the flow of an eddy along a smooth vertical or sloping side wall can arrest the propagation of boundary-trapped Kelvin waves when flow and waves are directed in opposition. At this point, a critical flow condition is reached that results in the generation of high-Rossby number unbalanced motions adjacent to the boundary. The ensuing boundary-trapped wave hydraulic control leads to elevated turbulent dissipation, which acts as sink of eddy energy. The condition that the along-boundary flow must oppose the direction of boundary-trapped wave propagation implies that this mechanism is only relevant for the dissipation of anticyclonic eddies. Using primitive equation numerical simulations, Cherian and Brink (2016) and (2018) studied the interactions between an anticyclonic eddy and a western boundary-like shelf break. They found that a complex interaction between the eddy and the shelf can result in the exchange of shelf and offshore waters, and a cascade of the mesoscale eddy structure into smaller-scale vortices.

Clément et al. (2016) analyzed observations from satellite altimetry and a bottom-mounted acoustic Doppler current profiler to assess the interaction between mesoscale eddies and the steep and rough topography offshore of the Bahamas, the same region studied in this manuscript. They documented near-bottom intensified northward flow during anticyclonic eddies at a depth of ~600 m, but no such intensification during cyclonic eddies. This near-bottom intensification in anticyclonic eddies was associated with an excitation of the internal wave field, particularly at superinertial frequencies associated with wave periods on the order of 3–10 h, with an associated increase in the rate of turbulent dissipation. Energy in the M_2 and near-inertial internal wave bands were comparatively low, except during two hurricanes captured by their time-series. From a global perspective, within the Atlantic, the conversion of M_2 tidal energy into the internal wave field as internal tides is relatively low (Vic et al., 2019). Further, using a semianalytical model for barotropic-to-baroclinic energy conversion, Fernández-Castro et al. (2020) show that in the study region discussed in this manuscript, energy conversion is minimal at $<10^{-4}$ W m^2 compared to values of $>10^{-2}$ W m^2 along the shelf to the north of our study region and within the Florida Straits. Thus, the analysis of Clément et al. (2016) suggested that offshore of the Bahamas mesoscale eddy energy is radiated away from the western boundary as internal waves, when the eddy flow impinges on the boundary. Their analysis and that of Fernández-Castro et al. (2020) both highlight that offshore of the Bahamas, tides, and winds do not play a leading role in setting the rate of turbulent dissipation.

There are many additional studies that have explored the more general problem of flow-topography interaction, and that are therefore relevant to the question of mesoscale eddy decay at western boundaries. For example, MacCready and Pawlak (2001) considered a flow along a corrugated slope using analytical and numerical methods. They differentiated between fast- and slow-flow regimes based on the ratio U/LN, where U is the along-slope flow speed, N is the buoyancy frequency, and L is the along-slope length scale. They showed that in the fast-flow regime fluid flows over the ridge, while in the slow-flow regime fluid follows isobaths. In the fast-flow regime, internal waves radiate energy away from the topography, and elevated turbulence and mixing occur in the lee of topographic obstacles. Expanding on the analysis of MacCready and Pawlak (2001), Warner and MacCready (2009) and (2014) investigated the flow past a sloping headland, using observations and numerical simulations. They showed that the generation of internal waves and wake eddies contribute almost equally to form drag, with direct implications for the energy extracted from the flow.

The relative roles of internal wave radiation and near-boundary processes in energy dissipation were also addressed by Klymak and Gregg (2004), in the context of a comprehensive observation-based study of tidal flow over a sill in a coastal fjord. These authors found that around one third of the energy lost from the impinging flow was dissipated locally to the sill, in the form of turbulence associated with shear instability and a hydraulic jump. The remaining two thirds was radiated away from the sill as internal waves. The significance of internal waves in the dissipation of mesoscale flows was discussed by Nikurashin and

Ferrari (2011) and Scott et al. (2011), who estimated that 20% of the global wind power input to the ocean circulation is transferred into internal lee waves. Especially intense internal wave generation occurs where geostrophic flow impinges on rough and steep topography. Thus, this process may play an important role in the dissipation of mesoscale eddy energy at western boundaries.

Most recently, several authors have highlighted the possible implication of submesoscale instabilities at topographic boundaries in the dissipation of energy from near-balanced flows. For example, Gula et al. (2015) and (2016) used high-resolution numerical simulations of the Gulf Stream to show that, on the Gulf Stream's cyclonic side, bottom drag increases lateral (cyclonic) shear and the flow becomes unstable to horizontal shear instability. This forms vortices over the South Atlantic Bight after the Gulf Stream separates from the Florida coast, extracting energy from the balanced flow. In turn, on the Gulf Stream's anticyclonic side near the Bahamas, they found that the flow becomes unstable to centrifugal instability as bottom drag generates negative potential vorticity (PV). The submesoscale motions resulting from these instabilities led to elevated turbulent dissipation in the model. The link between this range of submesoscale dynamics and intense dissipation was corroborated by A. C. Naveira Garabato et al. (2019) with observations in a deep western boundary current.

The study of A. C. Naveira Garabato et al. (2019) brings to the fore the possible importance of frictional processes in the bottom boundary layer in dissipating mesoscale eddies at sloping topography. In this environment, and on time scales at which rotation becomes important, there is an asymmetry in the response of the bottom Ekman layer depending on the direction of the along-slope flow relative to the direction of Kelvin wave propagation. When the along-slope flow is in the direction of Kelvin wave propagation, the resultant Ekman transport leads to a downslope advection of buoyancy and statically unstable conditions. When the along-slope flow is in opposition to the direction of Kelvin wave propagation, upslope advection of buoyancy results in a thinner Ekman layer and more stable conditions (Trowbridge & Lentz, 1991). The time scales of this cross-slope advection are shorter than the time taken for the Ekman layer to attain its final states. This difference in time scales results in a substantial initial transient phase, leading to the generation of conditions favorable to the generation of both submesoscale instabilities and internal waves (Brink & Lentz, 2009).

In summary, the diversity of dissipative processes unveiled by previous studies—for which the dynamics governing dissipation seemingly depend on specific details of each model simulation or case study—suggest that there may be a "zoo" of mechanisms implicated in the dissipation of mesoscale eddies at western boundaries. Here, we confirm and qualify this expectation with a targeted observational investigation of the dissipation of mesoscale eddies impinging on the western boundary off Great Abaco, Bahamas, in the North Atlantic Ocean, the same region studied by Clément et al. (2016). Using satellite altimetry, mooring measurements, and ship-based microstructure and velocity surveys, we illustrate the potential flow-topography interactions that extract energy from the eddy flows. We show that there may be a host of processes acting to dissipate eddies at the western boundary, both through direct flow-topography interactions and via remote downstream effects of the eddy's impingement on the topography. Some of the processes we observe are compatible with, and some are distinct from, those highlighted in the theoretical and modeling studies reviewed above.

2. Fieldwork and Data

2.1. Fieldwork

The data analyzed here were obtained as part of the Mechanisms Responsible for Mesoscale Eddy Energy Dissipation (MeRMEED) project. MeRMEED is a multiplatform observational program that aims to quantify the dissipative processes governing the decay of anticyclonic and cyclonic eddies at oceanic western boundaries. The MeRMEED observational campaign is composed of three parts: (1) Ship-based, acoustic current profiler (ADCP) and vertical microstructure profiler (VMP) surveys; (2) a 4-month autonomous glider survey; and (3) a 3-year enhancement of an existing Rapid Climate Change/Meridional Overturning Circulation and Heat flux Array (RAPID/MOCHA, hereinafter RAPID; McCarthy et al., 2015) mooring within the study region. MeRMEED focused on the interaction between eddies and the steep (1:2 to 3:4), rough slope offshore of Great Abaco, Bahamas (Figure 1). The work presented here primarily focuses on the ship-based surveys.

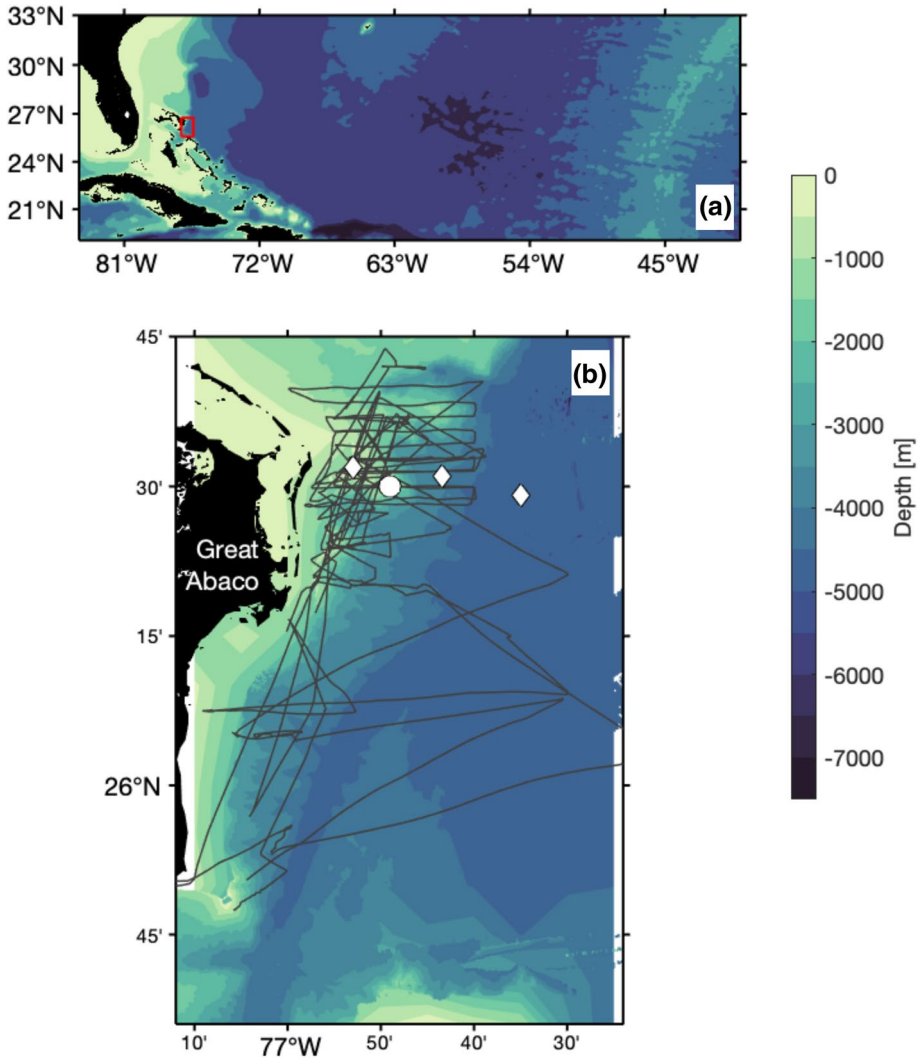

Figure 1. The Mechanisms Responsible for Mesoscale Eddy Energy Dissipation (MeRMEED) study region, shown in the context of the western subtropical North Atlantic (a), where the red box indicates the MeRMEED study area in (b). Gray lines delineate the cruise tracks from MeRMEED-1, MeRMEED-2, and MeRMEED-3. Markers show locations of the existing RAPID western boundary moorings along a protruding escarpment near 26.5°N. The white circle represents WB1, which was enhanced as part of MeRMEED with the addition of ADCPs and high-resolution thermistors. The colors in both panels show the bathymetry from TerrainBase. This is overlaid with multibeam bathymetric data. ADCPs, acoustic current profiler; RAPID, Rapid Climate Change.

The ship-based surveys were planned with the intention of capturing eddies of contrasting polarity, resulting in three short-duration cruises (10–15 days) aboard the *R/V F. G. Walton Smith*, during which we measured the along-slope flow structure and dissipation rate associated with different eddies. We refer to these cruises as MeRMEED-1 (1–7 December 2016), MeRMEED-2 (31 October to 10 November, 2017) and MeRMEED-3 (4–16 March 2018). During each of the cruises we performed a series of predominantly zonal transects, and we will discuss the results from some of these transects in Section 4. We describe the data collection and processing in the following sections.

2.2. Data and Processing

2.2.1. Vessel-Mounted ADCP

The *R/V F. G. Walton Smith* is equipped with a vessel-mounted RDI 75 kHz Ocean Surveyor ADCP. In narrowband mode this provided profiles of zonal and meridional velocity to a maximum depth of 750 m,

depending on the sea state. The ADCP was configured and run through the University of Hawai'i Data Acquisition System software suite, which provided automated processing and quality control. Data were available as 5-min averaged profiles. During an ADCP-only transect we typically steamed at 3.5–5 kts, giving an along-track resolution of up to 540 m. During VMP/ADCP transects, we achieved an along-track resolution of 150–310 m while steaming at a reduced speed of 1–2 kts.

2.2.2. Microstructure

During each of the MeRMEED cruises, we relied on free-falling microstructure profilers to provide a direct estimate of the rate of turbulent kinetic energy dissipation, ϵ, measured in units of W kg^{-1}. We used the tethered Rockland Scientific International VMP-2000. The VMP-2000 is attached to the vessel via a load-bearing data cable, enabling real-time collection of data. VMPs measure the vertical gradient of the turbulent fluctuations in velocity ($\partial u'/\partial z$) and temperature variance at centimeter scales. Assuming isotropy, ϵ is given by

$$\epsilon_{\text{micro}} = \frac{15\nu}{2}\overline{\left(\partial u' / \partial z\right)^2}, \tag{1}$$

where ν is the molecular viscosity and $\overline{\left(\partial u' / \partial z\right)^2}$, is the variance in the vertical gradient of turbulent fluctuations (Oakey, 1982).

VMP profiles were typically performed in a "tow-yo" fashion while the vessel steamed at ~1–2 kts, yielding a typical distance of 1.5–2 km between profiles. The VMP was ballasted to ensure free fall during the downcast at a target fall rate of 0.6 dbar s^{-1}. With a VMP sampling rate of 512 Hz, this fall rate allows the calculation of shear variance every ~0.6 dbar with 1 s bin widths. We subsequently bin-averaged the dissipation rate estimate onto a 2 dbar grid.

The processing of VMP profiles was conducted following the approach in A. Naveira Garabato (2009), as used by Sheen et al. (2013). Each instrument was deployed with two shear sensors. We selected either the primary or secondary sensor depending on which sensor consistently had the lowest noise level. The VMP was deployed with a pumped Seabird Electronics Conductivity-Temperature-Depth (CTD) sensor system including a SBE-3 temperature sensor and SBE-4 conductivity sensor sampling at 24 Hz. The CTD data was processed according to the manufacturer specifications, using recommended values for the cell thermal mass coefficients ($\alpha = 0.03$ and $\beta = 7.0$). We use data from the downcast only, bin-averaged to a 0.5 dbar grid. When plotting transects of CTD output, we linearly interpolate between adjacent profiles. We calculate potential density referenced to 0 dbar using the Gibbs Seawater toolkit (IOC et al., 2010).

2.2.3. Mooring Data

The fieldwork for MeRMEED included enhancement of the RAPID mooring WB1, with two additional 75 kHz ADCPs, providing full-depth velocity measurements. WB1 is deployed at 26.5°N, 76.8°W in ~1,400 m water depth (filled white circle; Figure 1b). The deployment spanned 18 months, from November 2015 to May 2017. These data were processed according to the methods outlined by Johns et al. (2008). The data provide context for the flow structure measured during MeRMEED-1, and allow the identification of additional anticyclonic and cyclonic eddies not sampled by ship-based surveys.

2.2.4. Additional Datasets

We use several additional datasets to aid in our interpretation of ship-based surveys. We show snapshots of sea level anomaly (SLA) data derived from gridded near real-time multimission satellite altimetry, acquired from the Copernicus Marine Environment Monitoring Service (http://marine.copernicus.eu/). From the daily global ocean gridded L4 sea surface heights and derived variables reprocessed product, we acquired the SLA variable with a 0.25° × 0.25° horizontal resolution. We use snapshots of sea surface temperature (SST) obtained from the Group for High Resolution SST (GHRSST) level 4 Multiscale Ultrahigh Resolution (MUR) global analysis, which incorporates measurements from multiple instruments to give a horizontal resolution of 0.01° × 0.01° (https://www.ghrsst.org/). Specific snapshots were chosen to represent the conditions of each individual cruise as follows: MeRMEED-1—November 24, 2016; MeRMEED-2—November 9, 2017; and MeRMEED-3—March 16, 2018. For detailed bathymetry within our study region, we use multibeam-based data acquired from the National Centers for Environmental Information (https://www.ncei.noaa.gov/).

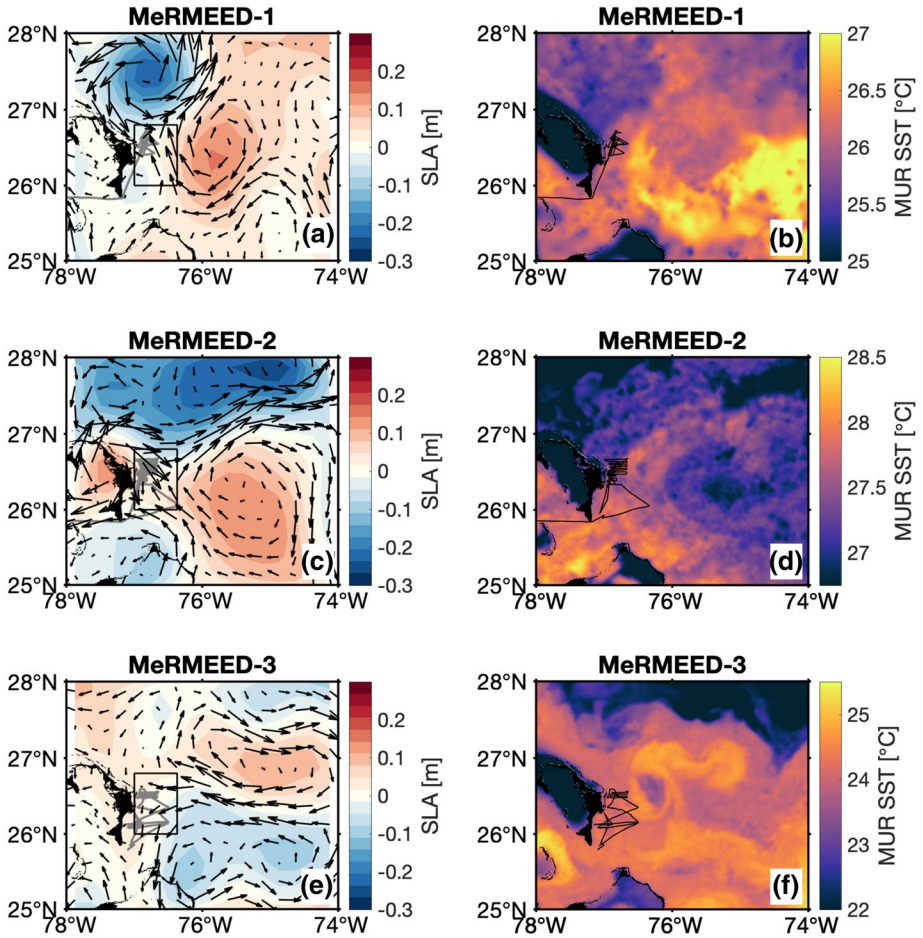

Figure 2. (a, c, e) Colors represent SLA during MeRMEED-1 (November 24, 2016), MeRMEED-2 (November 9, 2017), and MeRMEED-3 (March 16, 2018), respectively. Black arrows show surface geostrophic velocity estimated from SLA. Cruise tracks are indicated in gray. (b, d, f) MUR SST snapshots during MeRMEED-1, MeRMEED-2, and MeRMEED-3, respectively (units: °C; same dates as SLA), with cruise tracks shown in black. MeRMEED, Mechanisms Responsible for Mesoscale Eddy Energy Dissipation; MUR, Multiscale Ultrahigh Resolution; SLA, sea level anomaly; SST, sea surface temperature.

3. Eddy-Topography Interactions Near Great Abaco, Bahamas

3.1. Eddy-Topography Configuration

During MeRMEED-1 and MeRMEED-2, we sampled the western edges of two well-defined anticyclonic eddies (Figures 2a–2d), manifested in a northward flow along the slope in our study area. During MeRMEED-1, a weak anticyclonic eddy was positioned to the north-east of our study area, with the eddy core centered at 27°N, 76°W. According to SLA, this anticyclonic eddy was adjacent to a cyclonic eddy centered at 27.7°N, 77°W, with strong northward flow between the two eddies. This structure is also visible in high-resolution SST imagery (Figure 2b). Here, we see a thermal front—warm water to the south next to colder water to the north—that aligns with the velocity vectors derived from SLA.

We sampled an anticyclonic eddy of larger diameter during MeRMEED-2, with the core positioned at 26°N, 75°W. The resultant northward, along-slope flow within our study area led to a similar pattern of warm and cold SST to that observed during MeRMEED-1 (Figure 2d). However, the SST difference between the sampling region (cruise tracks in Figure 2d) and the eddy core appears larger in MeRMEED-2 than in MeRMEED-1. Separate analysis of MeRMEED glider data shows that the anticyclonic eddy observed during MeRMEED-2 is a mode water eddy (Fernández-Castro et al., 2020).

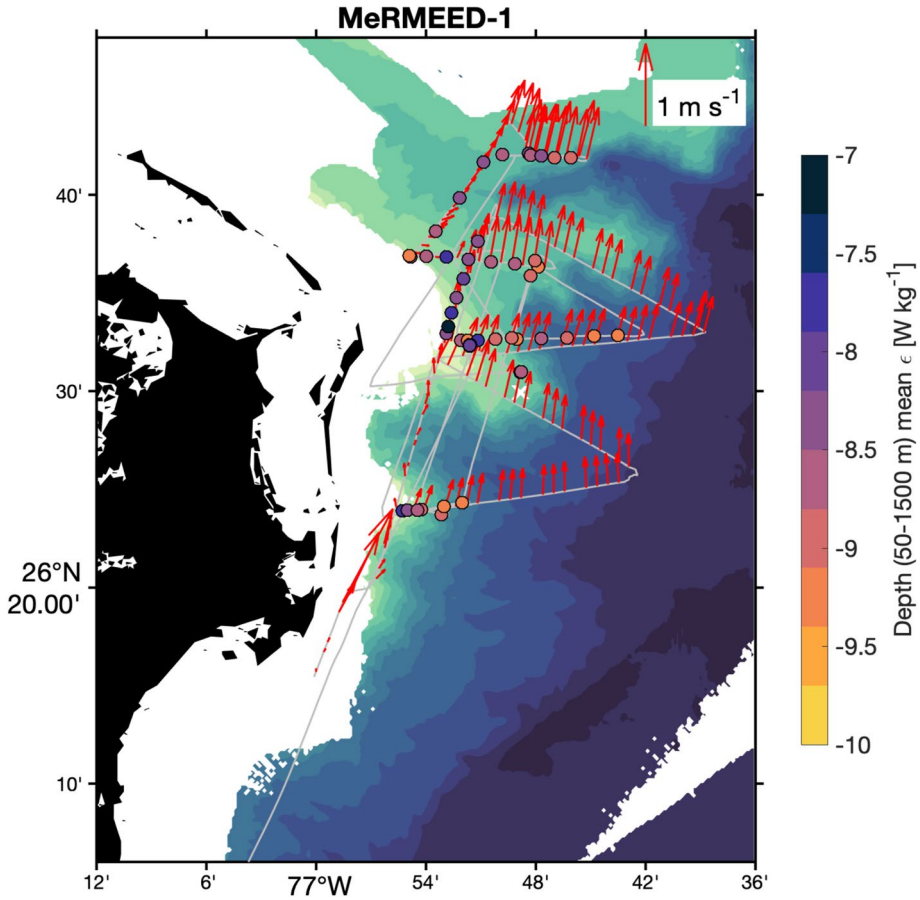

Figure 3. Cruise track from MeRMEED-1 (gray line) overlaid onto multibeam bathymetry (colors). Vectors show the depth- (surface to 700 m) averaged velocity from the vessel-mounted ADCP. MeRMEED-1 focused on the flow upstream and downstream of the protruding escarpment at 26.5°N, the location of WB1 (white cross). Colored markers show the depth mean VMP dissipation rate from MeRMEED-1. Note the logarithmic scale. Units: W kg^{-1}. Depth means are calculated as the vertical integral of the VMP dissipation rate between 50 m and the maximum depth of the profile, divided by the depth range between 50 and the maximum depth of the profile. ADCP, acoustic current profiler; MeRMEED, Mechanisms Responsible for Mesoscale Eddy Energy Dissipation; VMP, vertical microstructure profiler.

SLA during MeRMEED-3 indicates that a cyclonic eddy centered at 26°N, 75.5°W drives southward flow along the slope within our study area (Figure 2e). The high-resolution SST imagery shows an eddy-like feature in a slightly different position than indicated by SLA, with a cold core at 26.5°N, 76.25°W surrounded by warmer water (Figure 2f). The shape of the warmer water around cold core suggests cyclonic rotation. SST imagery from subsequent days indicates that this is a rapidly propagating eddy that moves northwestward from the position shown in Figure 2e to the north of Great Abaco.

Each of the MeRMEED cruises predominantly focused on flow upstream and downstream of a protruding escarpment at 26.5°N, along which RAPID moorings are currently deployed (Figures 3–5). Following the analysis of Clément et al. (2016), the contributions of the tidal- and wind-driven flow to the turbulent dissipation rate are assumed to be small compared to the eddy flow. The anticyclonic eddies sampled during MeRMEED-1 and MeRMEED-2 were characterized by northward flow both upstream and downstream of this escarpment, with a typical depth-averaged flow of 0.5 ms^{-1}. Maximum velocities exceeded 1 ms^{-1} downstream of the escarpment, as observed during MeRMEED-1. In this region, we also see evidence of horizontal shear with weaker flow to the west in the lee of the escarpment. There were a few instances of southward flow during MeRMEED-1 and MeRMEED-2, notably immediately south of the escarpment at 26.5°N within 2–3 km of the slope. The expected southward flow associated with the cyclonic eddy during MeRMEED-3 was not observed over the escarpment, where weak northward flow was still present. However, we did observe southward flow offshore of the slope, suggesting that the cyclonic eddy may not have

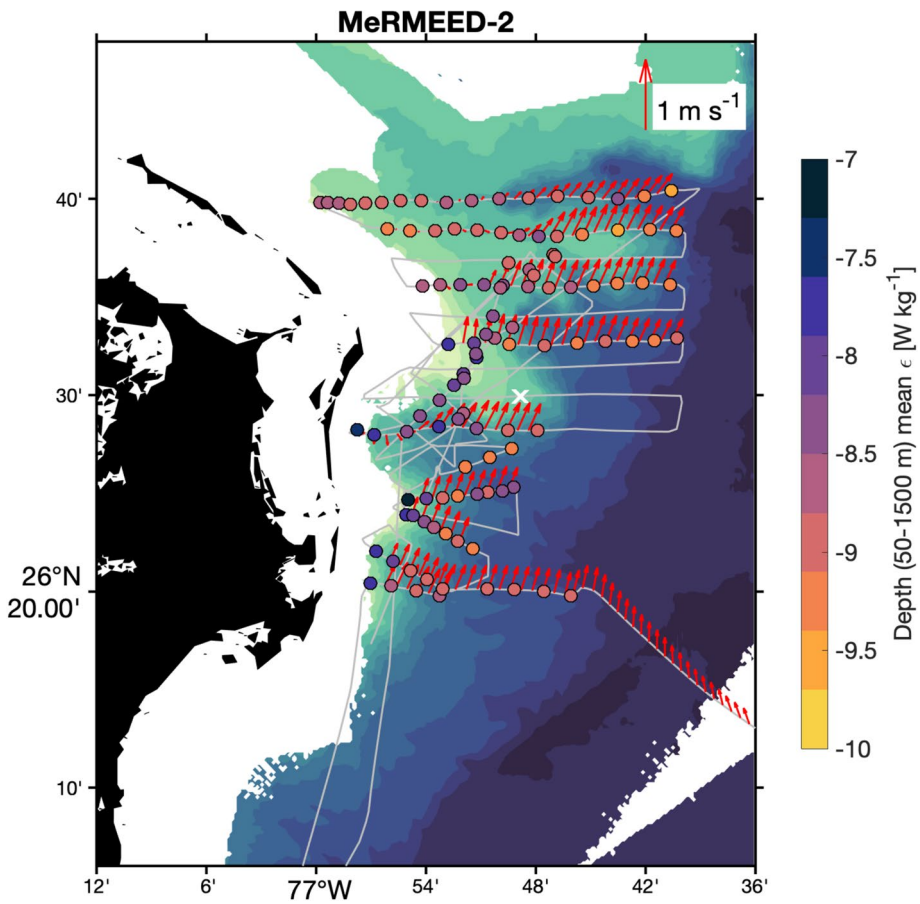

Figure 4. As in Figure 3, but for MeRMEED-2. Again, MeRMEED-2 focused on the flow upstream and downstream of the protruding escarpment at 26.5°N. MeRMEED, Mechanisms Responsible for Mesoscale Eddy Energy Dissipation.

been close enough to the slope to impact the flow there. This is supported by the position of the eddy-like feature visible in Figure 2e.

3.2. Elevated Near-Slope Turbulent Dissipation

Across three MeRMEED cruises, a total of 226 VMP profiles were collected. The locations of these profiles are shown in Figures 3–5, where the color of each profile position indicates the depth-mean dissipation rate:

$$\langle \epsilon \rangle_z = \frac{1}{H} \int_{z_{\max}}^{50\mathrm{m}} \epsilon \, \mathrm{d}z, \tag{2}$$

where $z_{\max}$ is the maximum depth of the VMP profile in meters and $H = z_{\max} - 50$. The VMP surveys during MeRMEED-1 (Figure 3) and MeRMEED-2 (Figure 4) focused on measuring turbulent dissipation within ±1/6° latitude of the escarpment at 26.5°N. With the northward flow associated with the anticyclonic eddies running along the slope and over the escarpment, $\langle \epsilon \rangle_z$ was generally elevated in the 2–3 profiles (1–2 km) closest to the slope. We also observed persistently elevated $\langle \epsilon \rangle_z$ just south of the escarpment, over the escarpment, and just to the north of the escarpment. In the following sections, we will discuss the potential mechanisms that may underpin this elevated dissipation.

During MeRMEED-3, despite observing much weaker northward flow along the slope, we still measured elevated $\langle \epsilon \rangle_z$ near the boundary, even in areas of very weak flow (e.g., near 26.35°N). In a later section, we

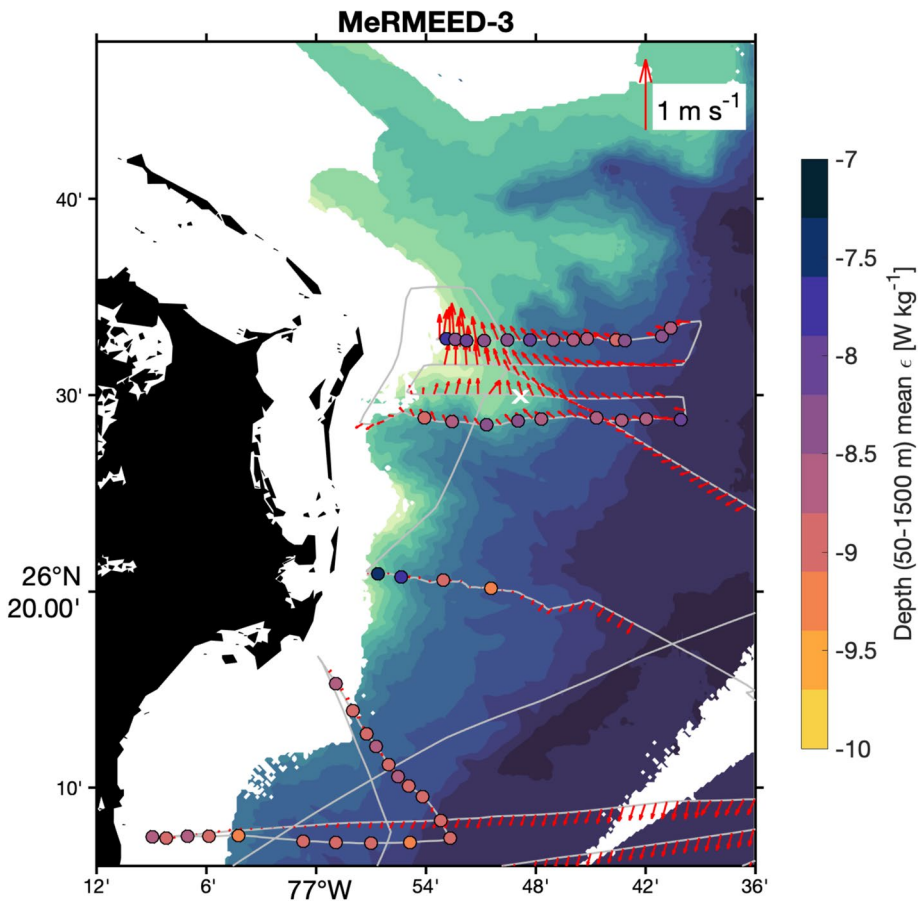

Figure 5. As in Figure 3, but for MeRMEED-3. In MeRMEED-3, we focused on the flow over the protruding escarpment at 26.5°N, and on defining the southward flow associated with the cyclonic eddy present during the cruise. MeRMEED, Mechanisms Responsible for Mesoscale Eddy Energy Dissipation.

will discuss this in the context of the data collected by the WB1 mooring, and of the analysis of Clément et al. (2016).

4. Topographic Controls on Mesoscale Eddy Energy Dissipation

During the MeRMEED cruises, we observed elevated dissipation of turbulent kinetic energy within 1–2 km of the slope and near a protruding escarpment at 26.5°N (Figures 3–5). In this section, we identify (to the extent that our data permit) the key processes responsible for the measured patterns of elevated dissipation. These processes include shear-driven instabilities, centrifugal instability, hydraulic control, and a potential case for Kelvin wave hydraulic control.

4.1. Horizontal Shear Instability in the Lee of Topography

In both anticyclonic eddies (MeRMEED-1 and MeRMEED-2), the largest velocities were found downstream (north) of the escarpment at 26.5°N. North of 26.5°N, the 1,000 m isobath turns sharply to the west. At this point, the along-slope flow associated with the anticyclonic eddies separated from the slope to flow in a northeastward direction (Figures 3 and 4). This is also manifested in the SST structure in this area, shown in Figures 2b and 2d.

The vertical structure of the flow in the region downstream of the escarpment was significantly modified from the expected first-mode baroclinic structure of mesoscale eddies (e.g., Wunsch, 1997). Zonal transects

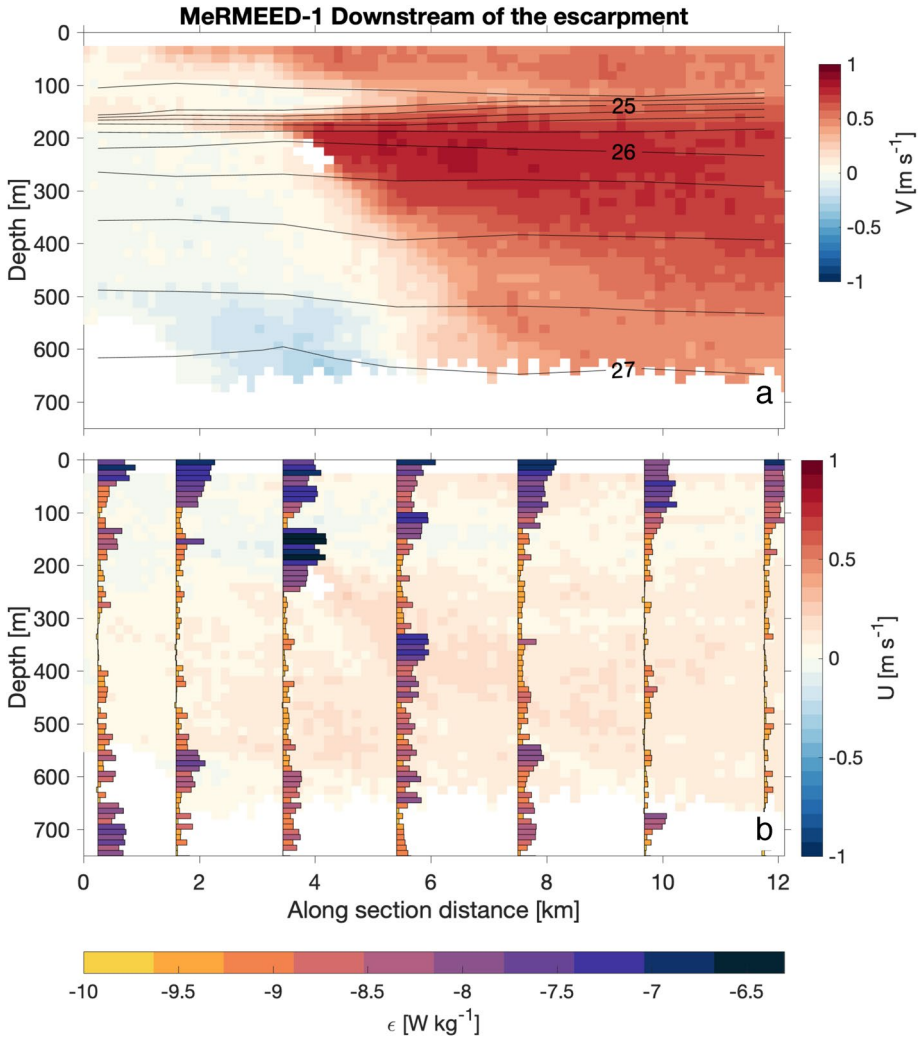

Figure 6. A zonal transect of (a) meridional and (b) zonal velocity from MeRMEED-1, downstream of the escarpment at 26.5°N (see inset plot in Figure 7). Units: m s^{-1}. Solid contours show potential density defined as σ_θ (units: kgm^{-3}). The stacked bar plots in panel (b) indicate VMP-based estimates of dissipation rate in 10 m bins. Each bar is scaled by 10^{-10} Wkg^{-1}. The color of each bar represents the dissipation rate, note the logarithmic scale. MeRMEED, Mechanisms Responsible for Mesoscale Eddy Energy Dissipation; VMP, vertical microstructure profiler.

of meridional and zonal velocity revealed intensified northward flow (Figure 6, from MeRMEED-1; see inset map in Figure 7) between 200 and 300 m, pinched between a shallower layer of weaker southwestward flow and a deeper layer of southeastward flow. The eddy's northeastward flow was intensified as it squeezed between these layers, with maximum values exceeding 1 ms^{-1} and layers of large vertical shear above and below.

Turbulent dissipation was elevated within the layers of large shear, reaching a maximum of 5.6×10^{-7} W kg^{-1} where the eddy's northeastward flow was at its thinnest (Figure 6b). The structure of the flow downstream of the escarpment at 26.5°N, and observed patterns of elevated turbulent dissipation shown in Figure 6, were encountered in additional transects during both MeRMEED-1 and MeRMEED-2, suggesting that these features are characteristic of anticyclonic eddies in this region.

The sheared layer between the eddy's northeastward flow and the deeper southeastward flow extends from 200 m at a distance of 4 km to 600 m at 7 km (Figure 6). This angle matches the slope of the escarpment at its shallowest point before the topography deepens and turns to the west. This is highlighted by comparing the angle of the sheared layer to zonal profiles of topography over the escarpment at 26.5°N (Figure 7). Thus, all

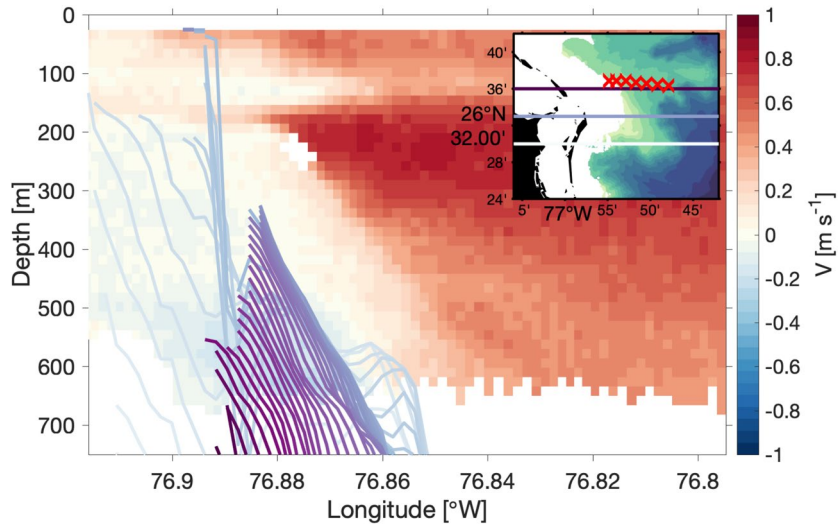

Figure 7. Meridional velocity downstream of the escarpment during MeRMEED-1 (units: m s^{-1}), overlaid with zonal profiles of topography between 26.4°N (white) and 26.7°N (purple; see inset plot). The inset plot shows the location of the transect (red crosses) with respect to the escarpment at 26.5°N. The zonal profiles of topography indicate that the slope of the sheared velocity layer to the north of the escarpment at 26.5°N closely matches the escarpment's topographic slope. MeRMEED, Mechanisms Responsible for Mesoscale Eddy Energy Dissipation.

available evidence suggests that this is an example of elevated turbulent dissipation due to flow-topography interactions in a region where the flow has separated from the slope.

To gain a deeper understanding of the processes responsible for the elevated turbulent dissipation found downstream of the escarpment at 26.5°N, we first compute the Richardson number (*Ri*):

$$Ri = \frac{N^2}{\left(\partial u / \partial z\right)^2 + \left(\partial v / \partial z\right)^2}, \tag{3}$$

where N is the buoyancy frequency, and the denominator is the squared vertical shear. A low *Ri* (typically $Ri < 0.25$) suggests that vertical shear is large enough to overcome the local stratification. Along the transect shown in Figure 6, *Ri* was consistently near 0.25 in the sheared layers between the northeastward eddy flow and the two layers of southward flow (Figure 8). This low-*Ri* features are aligned with the bands of elevated turbulent dissipation (particularly in the sheared layer set by the upstream topographic slope), indicating that some of the strong vertical shear in these layers drives intense dissipation.

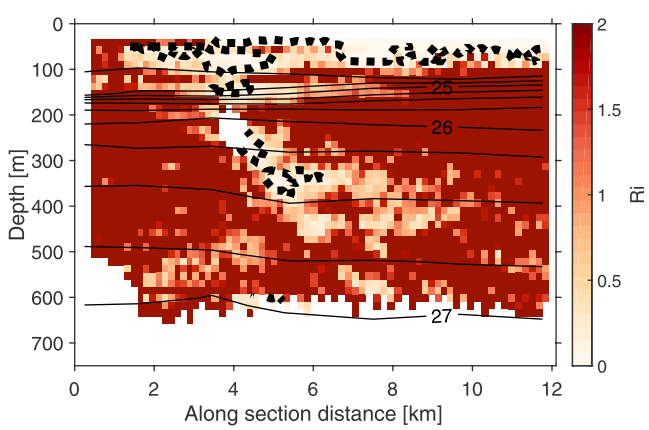

Figure 8. Richardson number (*Ri*) downstream of the escarpment during MeRMEED-1. Dashed contours show $Ri < 0.05$, selected to highlight regions of consistently low *Ri*. Solid contours denote potential density defined as σ_θ (units: kgm^{-3}). MeRMEED, Mechanisms Responsible for Mesoscale Eddy Energy Dissipation.

The occurrence of marked horizontal layers in velocity at depths shallower than 200 m suggests a lateral redistribution of fluid that cannot be explained by shear-driven turbulence alone. In Figure 6 at depths shallower than 200 m, we see a thin northeastward-flowing layer extending west from the core of the eddy's northeastward flow, below the layer of southwestward flow described above (which extends east above the core of the eddy flow). These layers correspond with bands of elevated dissipation between 100–150 m and west of 6 km, where *Ri* was variable (i.e., not consistently low).

Similar flow-topography interactions were documented by Gula et al. (2015), using both observations and a numerical model. These authors described how the cyclonic wall of the northward-flowing Gulf Stream separates from the shallow topography of the coast to the north of

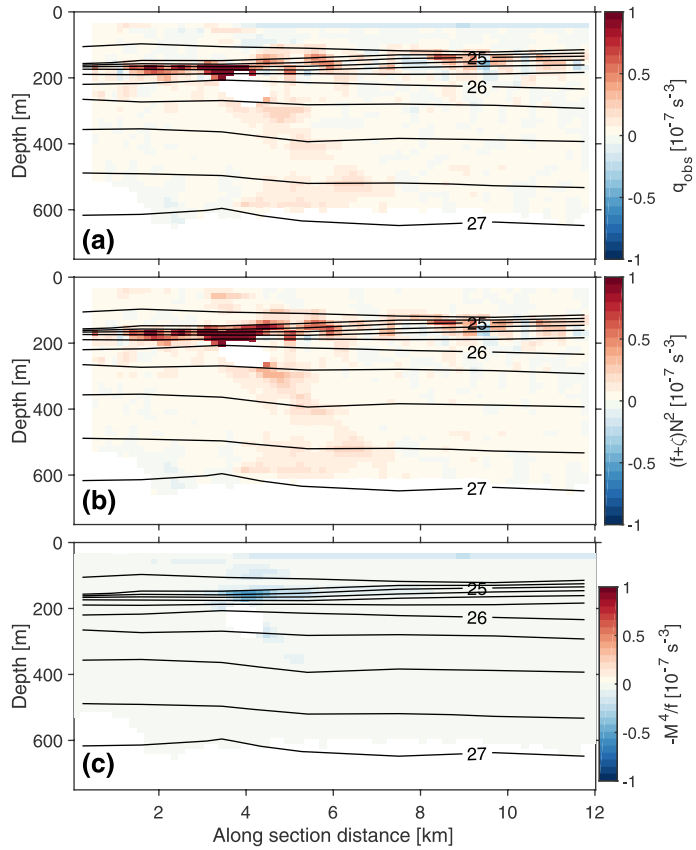

Figure 9. (a) Potential vorticity downstream of the escarpment during MeRMEED-1 (units: 10^{-7} s^{-2}). (b and c) The contribution by each term in Equation 4 to the total potential vorticity shown in (a). Black contours indicate potential density defined as σ_θ. MeRMEED, Mechanisms Responsible for Mesoscale Eddy Energy Dissipation.

the Florida Straits. As in Figure 6, Gula et al. (2015) found a separation from a boundary placed to the left of the flow. Following separation, they observed the generation of vortices due to horizontal shear instability, which extracts energy from the mean flow via horizontal shear production. The necessary condition for horizontal shear instability is a change in the sign of the PV gradient on an isopycnal (Vallis, 2017).

Following the approach of Thompson et al. (2016), we use an "observational" expression for PV (q_{obs}) along a transect derived from the full expression for Ertel PV (e.g., Hoskins, 1974):

$$q_{\text{obs}} = (f + \zeta)N^2 - M^4 / f, \tag{4}$$

where $f = 2\Omega\sin(\phi)$, Ω is the Earth's angular velocity, ϕ is latitude, ζ is the vertical relative vorticity, and $M^2 = b_x$ is the lateral buoyancy gradient (subscripts indicate partial derivatives). As in Thompson et al. (2016), we define ζ as the along-transect gradient of the cross-sectional velocity, since we can only compute gradients in this direction. The typical horizontal resolution of the ADCP velocity profiles was higher than that of the VMP-based buoyancy profiles. Assuming therefore that the flow is in geostrophic balance, we define $M^2 = b_x = fv_z$. A separate analysis (not shown) indicates that, to a good approximation, the geostrophic balance assumption holds.

The isopycnal gradient of PV downstream of the escarpment during MeRMEED-1 does exhibit a change in sign (Figure 9), as in similarly located transects from MeRMEED-2. This change in isopyncal PV gradient was evident at 200 m and 4 km in Figure 9, with predominantly positive PV along the shear layer where the northeastward flow is narrowest, flanked by areas of weak-magnitude PV. This PV distribution yields opposing signs of the isopycnal gradient of PV around the area of maximum PV, indicating conditions favorable to the development of horizontal shear instability. The layering described above is suggestive of the lateral

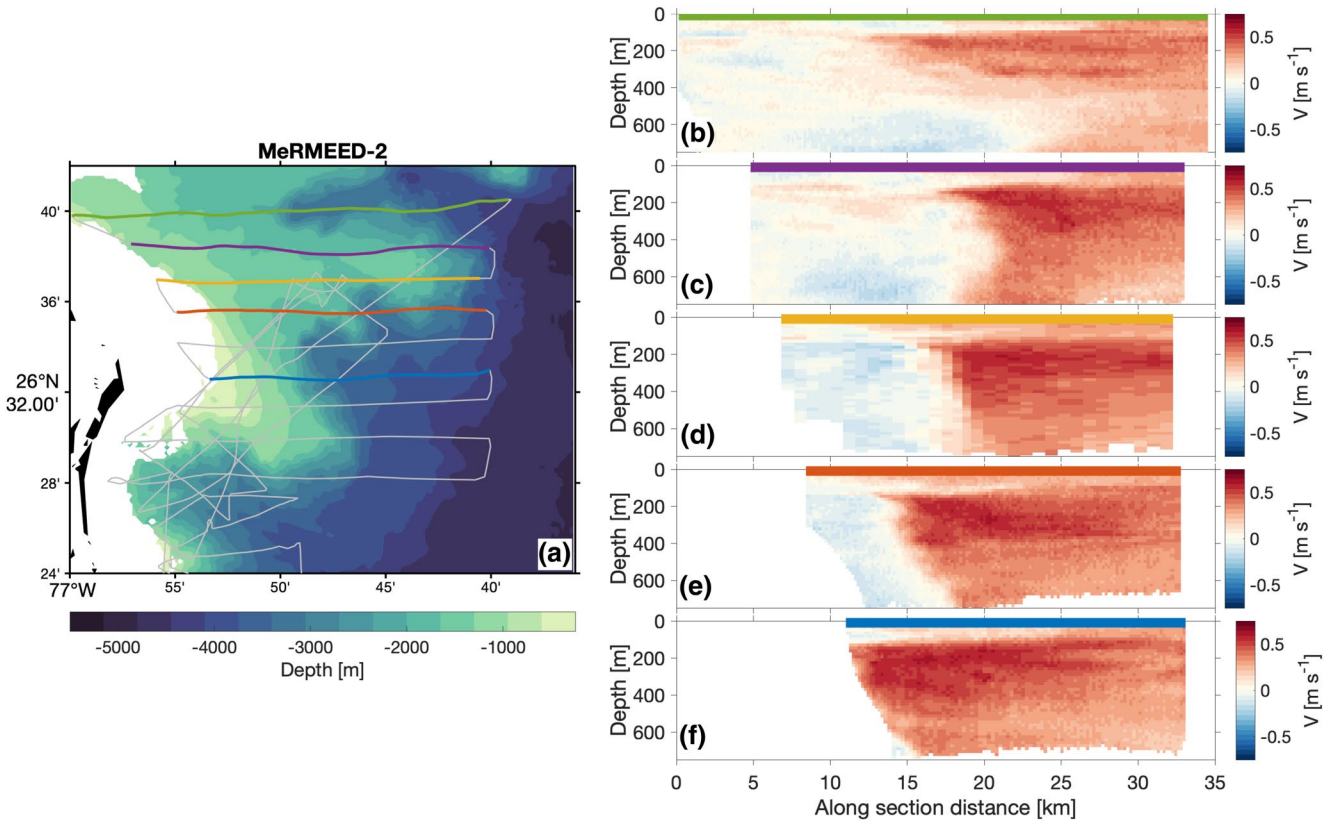

Figure 10. (a) MeRMEED-2 cruise track overlaid on multibeam bathymetry. Colored lines correspond to the sections of ADCP-based meridional velocity shown in (b)–(f). Units: m s^{-1}. ADCP, acoustic current profiler; MeRMEED, Mechanisms Responsible for Mesoscale Eddy Energy Dissipation.

exchange of fluid expected to occur during vortex formation by horizontal shear instability, which would act to erode PV gradients and thereby return the flow to a state of marginal stability. During MeRMEED-2, we performed a series of zonal transects downstream of the escarpment, separated by 3–4 km. These transects show a reduction in the maximum velocity and a gradual erosion of the strong shear between the eddy flow and the surrounding fluid (Figure 10), consistent with a progressive restoring of stable conditions with distance from the escarpment.

4.2. Topographic Steering and Centrifugal Instability

In the anticyclonic eddy sampled by MeRMEED-2, we observed an apparent recirculation of the eddy's northward flow immediately upstream of the escarpment at 26.5°N, associated either with a downstream recirculation or upstream flow blocking. While some of this northward flow continues over the escarpment, this southward recirculation can be observed in a westward indentation of the slope (Figure 11). This presents the possibility for the generation of negative PV, associated with anticyclonic vorticity and topography to the right of the flow. A similar flow-topography configuration is described by Gula et al. (2016), who find strong dissipation induced by centrifugal instability in a numerical model.

During MeRMEED-2, we performed a VMP transect through the center of the westward indentation in the slope (yellow circles; Figure 11). There, we observed some of the highest depth-mean turbulent dissipation rates for that cruise (Figure 4). The vertical and zonal structure of the flow through the indentation in the slope shows the eddy's northeastward flow to the east and the southward return flow to the west of 76.9°W (Figure 12). The northeastward flow was strongest between 100 and 400 m, and the southward return flow was most pronounced in the upper 400 m. Imprinted over this background flow structure are layers of northeastward flow at 100 and 300 m, and southwestward flow at 200 and 350 m. These layers are particularly clear at the western end of the transect, and extend as far east as 5 km (Figure 12). Turbulent

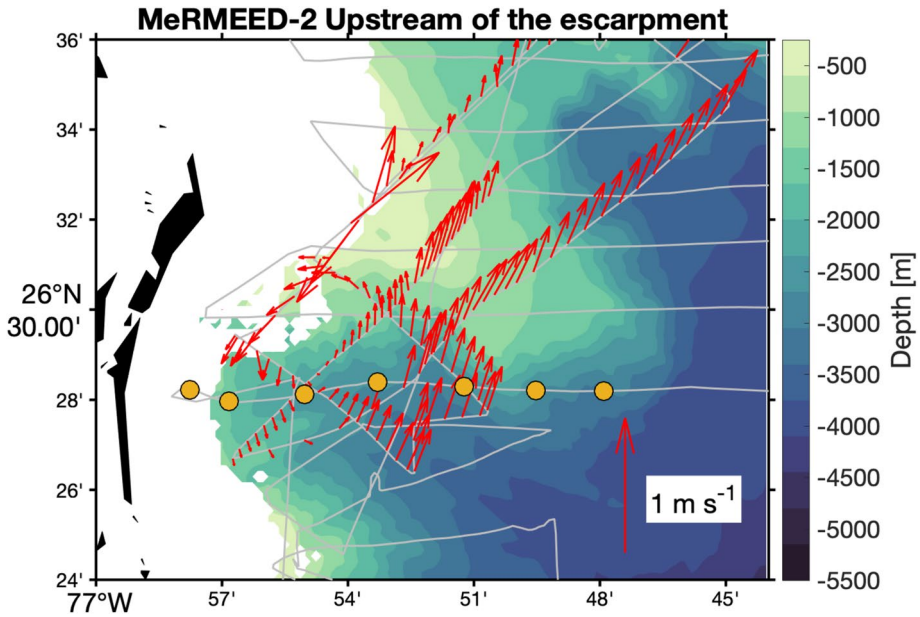

Figure 11. Overview of the flow upstream of the escarpment at 26.5°N in MeRMEED-2, showing a transect within an indentation in the slope (yellow markers). Vectors represent the depth-averaged velocity (units: m s^{-1}). These show that some of the flow is steered by the escarpment, resulting in southward flow within the indentation upstream of the escarpment. MeRMEED, Mechanisms Responsible for Mesoscale Eddy Energy Dissipation.

dissipation was highest within the southward return flow, particularly in the upper 400 m (Figure 12b) where we also observed layered flow structures.

To constrain the mechanism underpinning the measured increase in turbulent dissipation within the recirculation, we again compute PV (Figure 13). If, as in Gula et al. (2016), centrifugal instability is responsible for the elevated dissipation shown in Figure 12, we would expect to find negative PV associated with anticyclonic vorticity. Figure 13 confirms this expectation: a region of negative PV occurs within 2–3 km of the slope, flanked by an area of positive PV between the eddy's northeastward flow and the southward recirculation. Figure 13b shows that the negative PV is dominated by the second term in Equation 4, which accounts for the vertical component of relative vorticity. To explain the anomalous layers observed to the west of 76.92°W, we suggest that, in order to balance the generation of negative PV at the boundary and restore marginal stability, fluid is redistributed laterally along isopycnals. Thus, fluid with positive PV is transported westward and fluid with negative PV is transported eastward, increasing vertical shear and turbulent dissipation in the process.

4.3. Hydraulic Control and Internal Wave Generation

Clément et al. (2016) discussed the generation of internal waves when eddies impinge on the topographic slope of our study area. Their analysis focused on the RAPID moorings deployed along the escarpment at 26.5°N. In particular, they used a bottom-mounted ADCP deployed in a water depth of 600 m to show that elevated internal wave activity and turbulent dissipation occur during anticyclonic eddies, as a result of a bottom-intensified flow. During MeRMEED-1 and MeRMEED-2, we performed a series of measurements on and across the escarpment in the proximity of the bottom-mounted ADCP, to explore the mechanisms responsible for the results presented in Clément et al. (2016).

As part of MeRMEED-1 and MeRMEED-2, we sampled two different anticyclonic eddies (Figures 2a and 2c) that were associated with northeastward flow over the escarpment at 26.5°N (Figures 3 and 4). During MeRMEED-1, we performed a 12-h time series of VMP casts at the location of the bottom-mounted ADCP considered by Clément et al. (2016), while using the vessel-mounted ADCP to measure velocity (Figure 14; the orange diamond shows the time-series and bottom-mounted ADCP location). In addition,

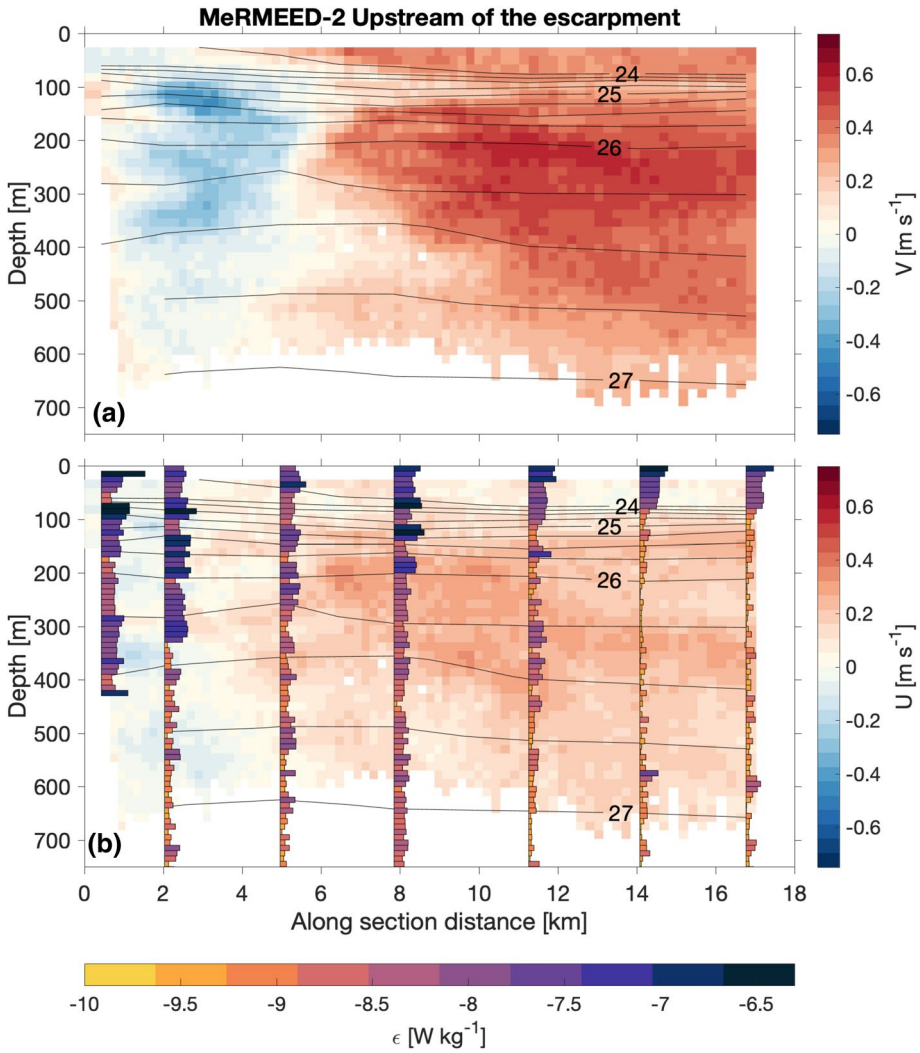

Figure 12. (a) Meridional and (b) zonal velocity from MeRMEED-2 upstream of the escarpment at 26.5°N. Units: m s^{-1}. The stacked bar plots in panel (b) show VMP-based estimates of dissipation rate in 10 m bins. Each bar is scaled by 10^{-10} Wkg^{-1}. The color of each bar represents the dissipation rate, note the logarithmic scale. MeRMEED, Mechanisms Responsible for Mesoscale Eddy Energy Dissipation; VPM, vertical microstructure profiler.

during MeRMEED-2 we performed a VMP and ADCP transect across the ridge of the escarpment, from southwest to northeast, which ran close to the bottom-mounted ADCP (Figure 14; blue markers show VMP cast locations). We will first discuss the data from the 12-h time series collected during MeRMEED-1.

The time series of horizontal velocity anomaly (with respect to the depth-mean profile) from MeRMEED-1 reveals slanted bands of velocity anomalies indicative of internal waves with downward phase velocity (dashed black lines show phase lines of successive wave crests in Figure 15a), upward group velocity and, therefore, upward energy propagation (Figure 15). This upward energy propagation suggests that the internal waves are generated at the bottom. Clément et al. (2016) noted that the 3–10 h period band was particularly energized during anticyclonic eddies; however, a more detailed comparison was not possible as no overlapping mooring data was available in this location due to instrument failure. Turbulent dissipation was highest near the bottom (Figure 15b; water depth ~720 m), with maximum values exceeding 5.6×10^{-7} W kg^{-1}. There are also some smaller mid-depth peaks in turbulent dissipation at zero-crossings of velocity that are as high as 1×10^{-8} W kg^{-1}.

To gain further insight into the processes generating near-bottom turbulence and upward-propagating internal waves, we measured the flow and turbulent dissipation in a southwest-to-northeast transect across

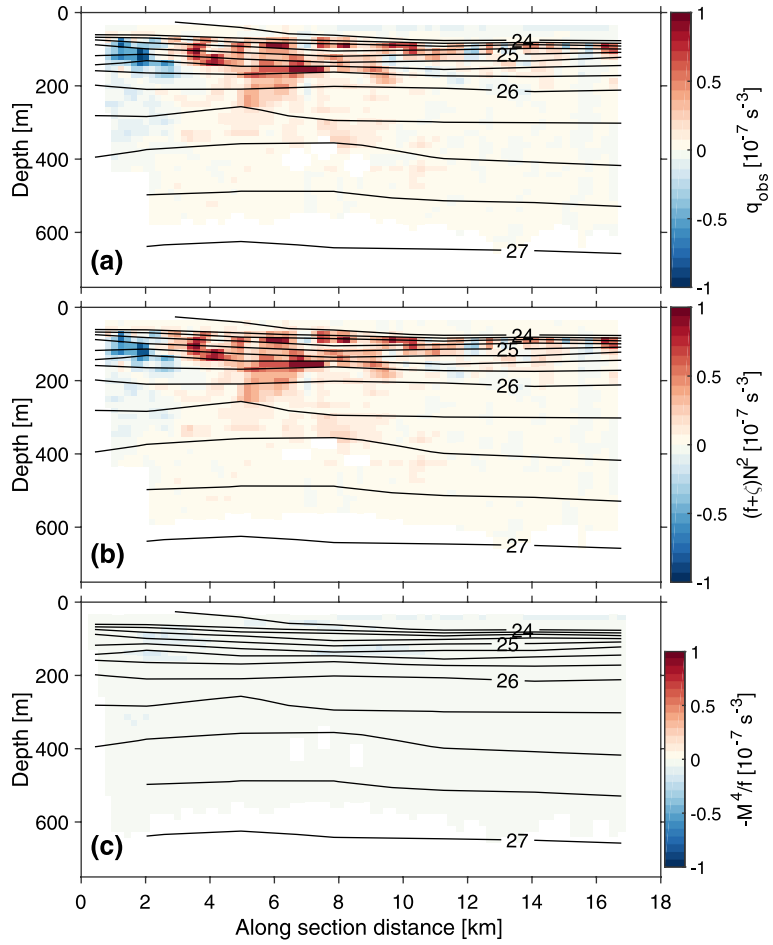

Figure 13. (a) Potential vorticity along MeRMEED-2 upstream of the escarpment at 26.5°N (units: 10^{-7} s^{-2}). (b and c) The contribution by each term in Equation 4 to the potential vorticity shown in (a). Black contours indicate potential density defined as σ_θ. MeRMEED, Mechanisms Responsible for Mesoscale Eddy Energy Dissipation.

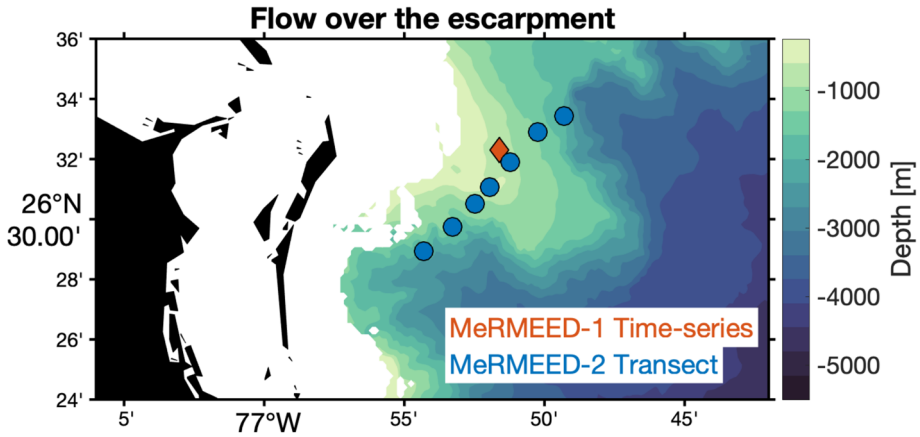

Figure 14. Map showing the location of a time series and a transect performed over the escarpment at 26.5°N during MeRMEED-1 and MeRMEED-2, respectively. MeRMEED, Mechanisms Responsible for Mesoscale Eddy Energy Dissipation.

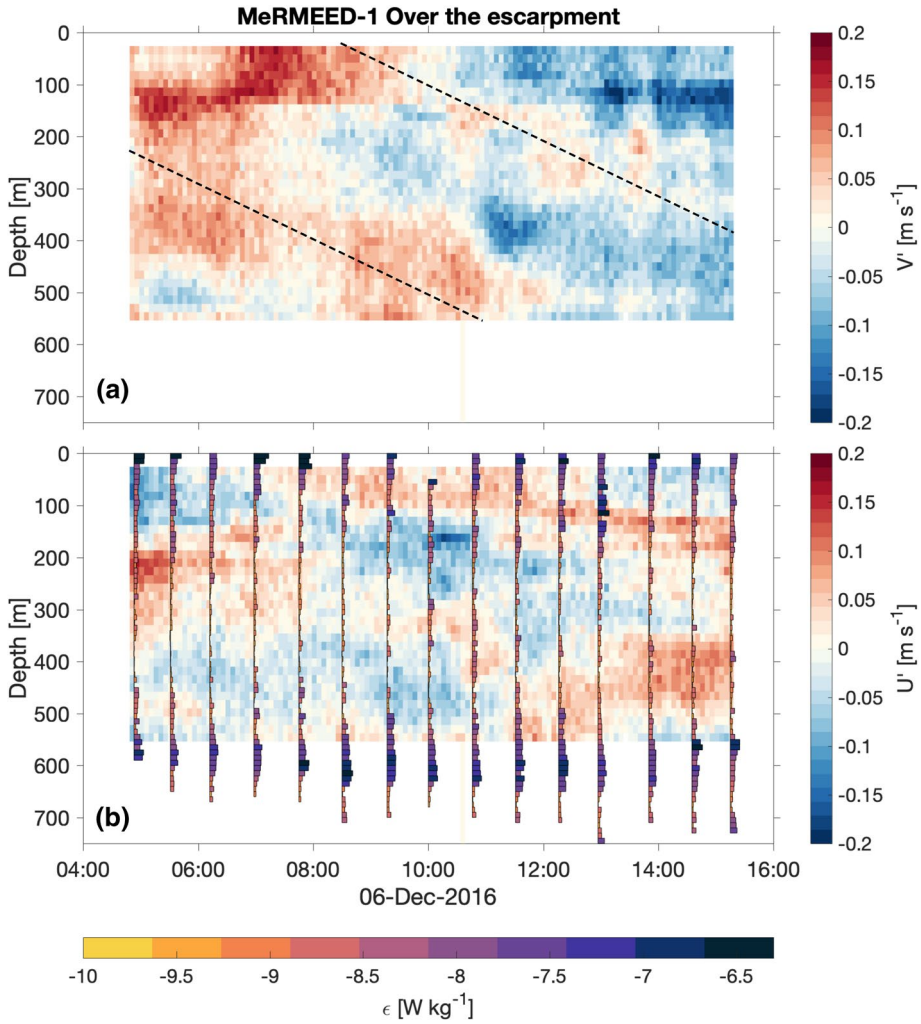

Figure 15. Time series of (a) meridional and (b) zonal velocity anomaly (with respect to their time-mean profile), suggesting downward phase propagation and upward energy propagation consistent with bottom-generated internal waves. Units: m s^{-1}. Water depth at this location was ~720 m. The dashed lines in panel (a) highlight potential wave crests. Panel (b) also shows profiles of VMP-based dissipation rate, as displayed in Figure 6. VPM, vertical microstructure profiler.

the escarpment during MeRMEED-2 (Figure 16). The eddy's northeastward flow is strongest between 100 and 300 m (Figures 16a and 16b). There is also some intensification of this northeastward flow on the downstream side of the escarpment. However, while the transect was intended to follow the major axis of the flow, small deviations from the along-stream direction may manifest as changes in flow intensity along the transect. The topographic steering of the flow described in Section 4.2 is clearly visible on the upstream side of the escarpment (westward flow below 500 m in Figure 16c); 500 m corresponds to the shallowest depth of the escarpment along this transect. The configuration of isopycnal surfaces is qualitatively consistent with hydraulically controlled flow (Dossmann et al., 2016), with a presumed hydraulic transition near the crest of the escarpment where incropping of isopycnals is observed, and an inflection in isopycnals downstream and above the escarpment (7.5 km and 500 m in Figure 16b). These spatial variations in isopycnal surfaces are indicative of internal wave radiation, which can also be seen in the component of velocity perpendicular to the orientation of the transect (Figure 17). Positive velocity anomalies are observed to radiate upwards, away from the escarpment, in both the upstream and downstream directions. The generation of these internal waves is likely linked to the back and forth movement of the hydraulic transition between the crest of the escarpment and deeper water around the escarpment, enabled by time dependence in the flow.

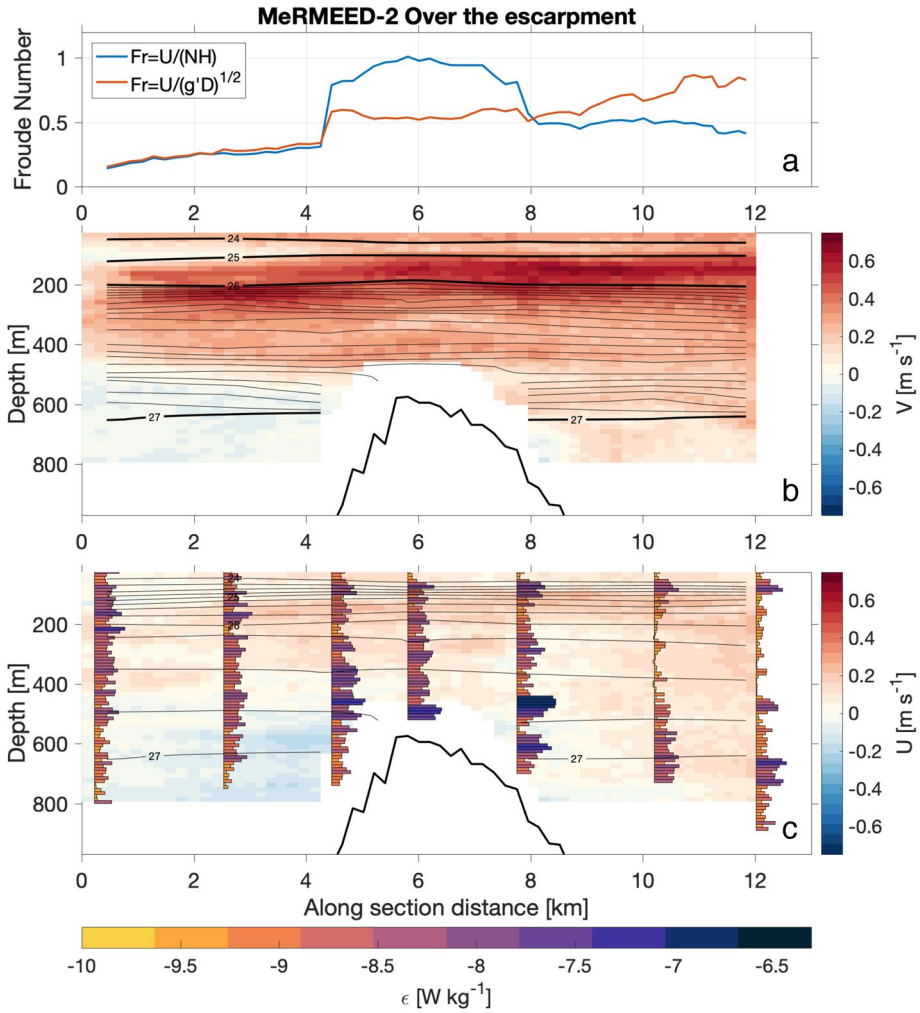

Figure 16. (a) Froude number, calculated following St Laurent and Thurnherr (2007) and Girton et al. (2006), over the escarpment at 26.5°N during MeRMEED-2. (b and c) Meridional and zonal velocity from MeRMEED-2. Units: m s^{-1}. Black contours show potential density defined as σ_θ (units: kgm^{-3}). Panel (c) also shows profiles of VMP-based dissipation rate, as displayed in Figure 6. MeRMEED, Mechanisms Responsible for Mesoscale Eddy Energy Dissipation; VPM, vertical microstructure profiler.

The possibility that flow over the escarpment may be hydraulically controlled is examined by calculating the Froude number in two ways: as $Fr = V/(ND)$ (St Laurent & Thurnherr, 2007) and as $Fr = V'/(g'D)^{1/2}$ (Girton et al., 2006). Here V is the component of velocity along the transect, and D the layer thickness from either 800 m or the seabed to the $\sigma_\theta = 25.25$ kgm^{-3} isopycnal. The terms V' and g' are defined as $V' = \left[\int_d^{d+D} V(z)\,dz\right] / D$ and $g' = g / \rho D \int_d^{d+D} \rho'(z)\,dz$, where d is either at 800 m or the seabed (whichever is shallower) and ρ' is the density anomaly relative to the background density away from the flow. These Froude number calculations are based on relatively arbitrary choices, so their interpretation remains ambiguous. At any rate, both Froude numbers increase over and downstream of the escarpment (Figure 16a), as would be expected from hydraulic control.

Alternatively, the problem can be framed in terms of the energy required by the flow to get over the escarpment. In this sense, the kinetic energy of the flow, V^2, must exchange for the potential energy required to get over the escarpment, given by N^2h^2, where h is the height of the escarpment. This becomes difficult to interpret when the escarpment is several thousands of meters tall. Instead we can ask how far below the crest of the escarpment is the flow blocked, or what is the vertical response of the flow to the escarpment. Assuming the topographic Froude number, $Nh/V >> 1$, we can approximate this vertical length scale as $\lambda \sim \pi V_0/N_0$

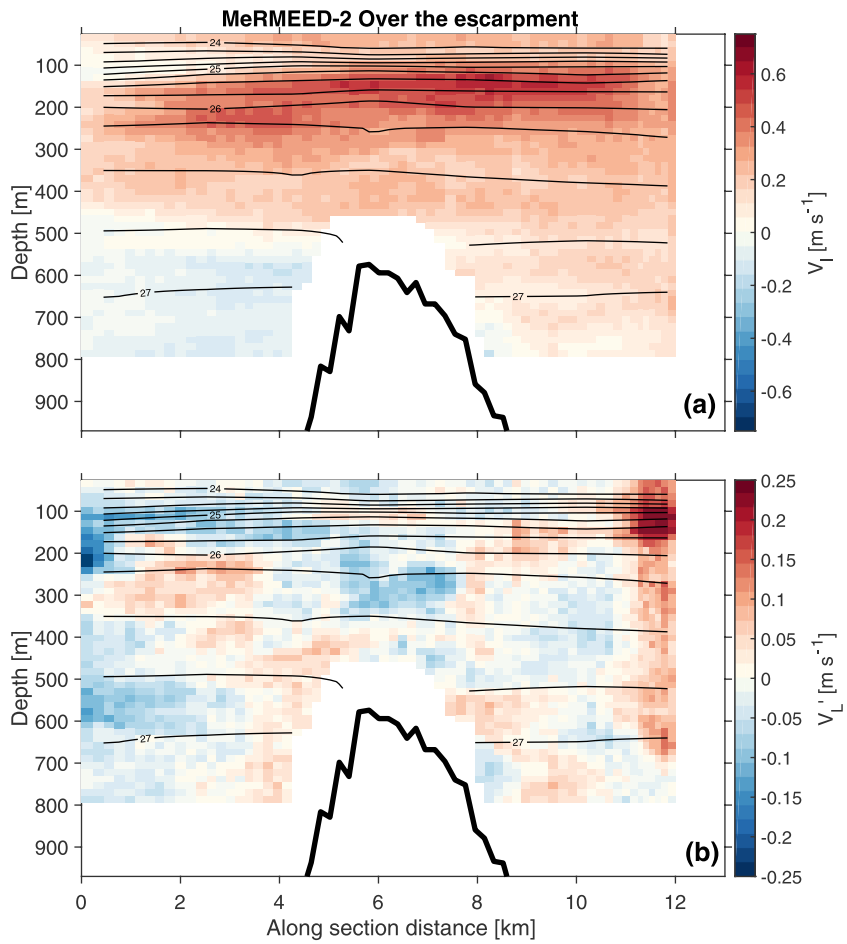

Figure 17. Components of velocity (a) parallel and (b) perpendicular to the transect over the escarpment at 26.5°N during MeRMEED-2. Units: m s^{-1}. Black contours show potential density defined as σ_θ (units: kgm^{-3}). The dashed black lines highlight the patterns of anomalous perpendicular velocity. MeRMEED, Mechanisms Responsible for Mesoscale Eddy Energy Dissipation.

(Klymak et al., 2010), where V_0 and N_0 are the velocity and stratification in the unblocked layer upstream of the escarpment. These fall within the range $0.1 < V_0 < 0.15$ ms^{-1} and $4.1 \times 10^{-3} < N_0 < 4.2 \times 10^{-3}$ s^{-1}. The yields a vertical length scale in the range of 75–110 m. Unfortunately, we have few observations this close to the bottom, likely limiting our ability to observe a hydraulic transition of this scale. A further comparison can be made between the advective time scale of the flow, V/L, and f, where L is the horizontal lengthscale of the escarpment. With $L = 2{,}000$ m, $V/L \sim 1.5 \times 10^{-4}$ s^{-1}, suggesting that the flow is likely to go over the escarpment, rather than around it. This, again, is compatible with the occurrence of a hydraulic transition over the escarpment.

Turbulent dissipation is highest in the three VMP profiles just upstream, over, and just downstream of the escarpment (Figure 16). The latter profile is less than 1 km from the position of the time series measurements shown in Figure 15, where we observed similarly elevated near-bottom turbulent dissipation. Turbulent dissipation is also enhanced between 400 and 800 m in the two northern-most profiles of the transect. All in all, our finding of enhanced turbulence and elevated Froude numbers over and downstream of the escarpment are suggestive of hydraulically controlled flow and a hydraulic jump.

4.4. Persistent Near-Slope Dissipation

A persistent feature through each of the MeRMEED cruises is the occurrence of elevated turbulent dissipation within 1–2 km of the 1,000 m isobath, where we observe northward along-slope flow consistently

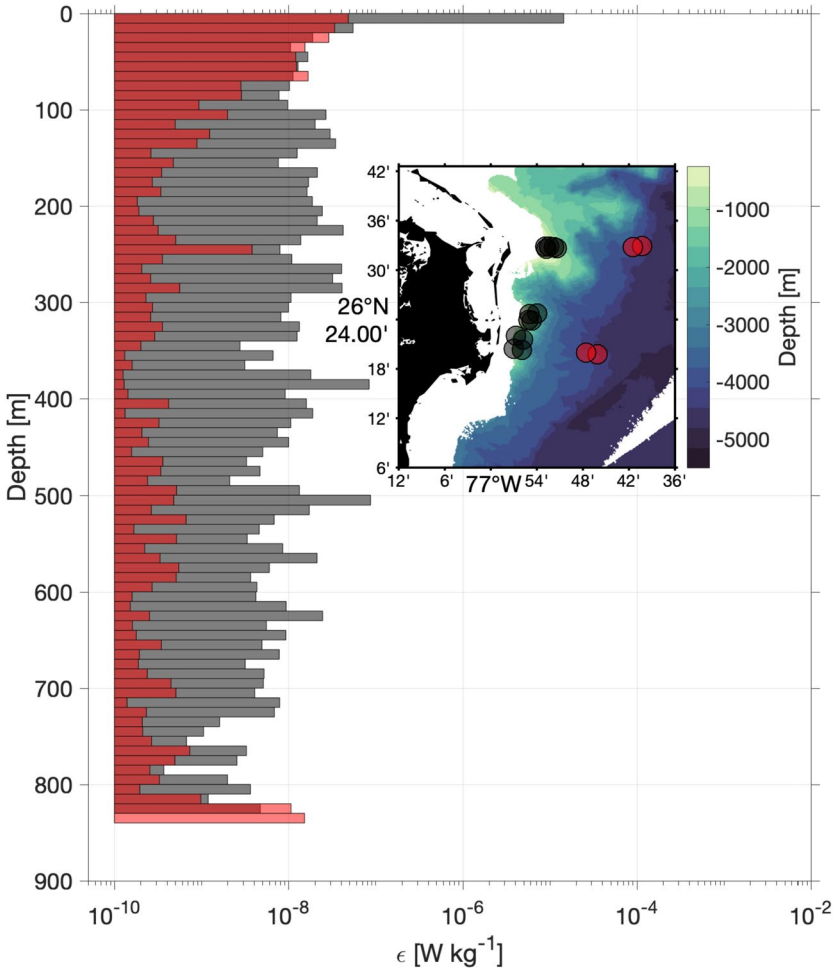

Figure 18. Mean profiles of on-slope (gray) and off-slope (red) VMP-based estimates of dissipation rate in 10 m bins, highlighting elevated mixing immediately adjacent to the shallow and steep topography. The inset map indicates the location of the profiles used to calculate the respective means. VPM, vertical microstructure profiler.

greater than 0.5 m s^{-1}. For example, near-boundary turbulent dissipation was elevated in several zonal VMP transects near 26.4°N in all three cruises (Figures 3–5). An average of these profiles (inset map; Figure 18) shows consistently elevated turbulent dissipation through the full water column (Figure 18) compared to profiles up to 10 km from the slope.

The elevated turbulence in these near-slope profiles does not directly correspond to any of the processes discussed above. A common feature of these profiles is an increase in Rossby number, defined as $Ro = v_x/f$, next to the boundary (Figure 19). In Figure 19, we show the root-mean-square Rossby number and turbulent dissipation averaged over the 6 transects near the slope in Figure 19. To construct an average, distances along transects were computed relative to the 1,000 m isobath, and ADCP data were interpolated to a cross-slope distance grid with 250 m horizontal resolution. VMP profiles were gridded to a 1 km resolution. These elevated Rossby numbers are indicative of intensified unbalanced motions adjacent to the boundary. In these transects, we also observe increased variability in PV adjacent to the boundary, reflecting large changes in relative vorticity, vertical shear, and stratification (not shown).

There are many processes that could be responsible for this elevated near-boundary dissipation and Rossby number. One such process is boundary-trapped Kelvin wave hydraulic control (Dewar & Hogg, 2010; Dewar et al., 2011; Hogg et al., 2011). If the northward along-slope eddy flow is sufficiently large to arrest southward-propagating Kelvin waves, this may induce supercritical flow and, subsequently, generate unbalanced motions. These unbalanced motions are more easily dissipated, thus extracting energy from

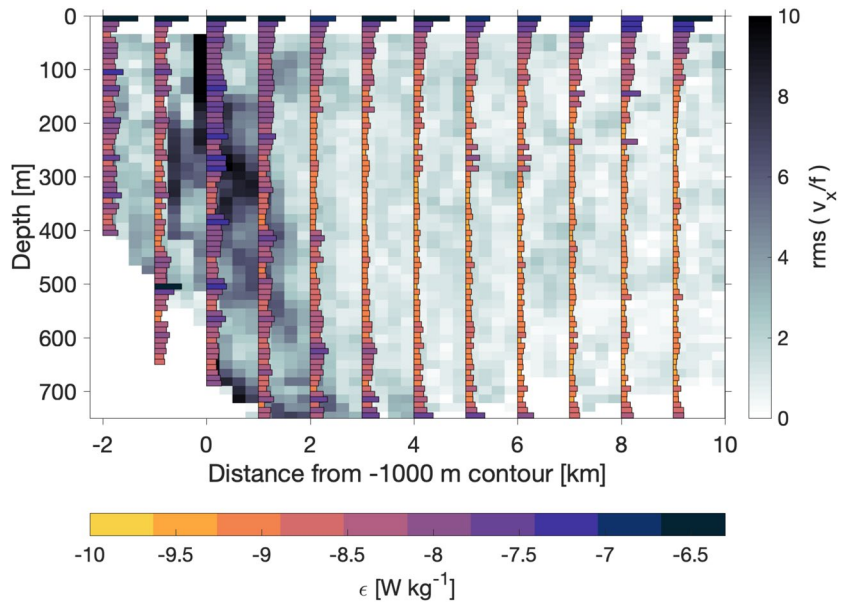

Figure 19. Root-mean-square (rms) Rossby number ($Ro = v_x/f$; Hogg et al., 2011), calculated using the sections starting from the on-slope profiles shown in Figure 18. The horizontal axis denotes the distance from the 1,000 m depth contour. The stacked bar plots show mean VMP-based estimates of dissipation rate in 10 m bins. Each bar is scaled by 10^{-10} Wkg^{-1}. The color of each bar represents the dissipation rate, note the logarithmic scale. VPM, vertical microstructure profiler.

the eddy's balanced flow. According to the analyses of Dewar and Hogg (2010); Dewar et al. (2011); Hogg et al. (2011), when the flow becomes supercritical, isopycnal surfaces begin to stretch and pinch within a few kilometers of the boundary, leading to the generation of unbalanced motions that manifest as elevated Rossby number. We observe similar conditions along the slope in our MeRMEED measurements. There are, however, other potential explanations for the persistent near-slope dissipation in our data, including the breaking of locally generated internal tides (Vic et al., 2019), the scattering of internal waves at the slope (MacKinnon et al., 2017), or the development of submesoscale instabilities not considered in our analysis (e.g., ageostrophic anticyclonic instability [McWilliams et al., 2004]).

5. Wider Context for Cruise Data

The MeRMEED cruise data provide snapshots of the turbulent processes occurring during two different anticyclonic eddies (MeRMEED-1, Figures 2a and 2b; MeRMEED-2, Figures 2c and 2d) and a cyclonic eddy (MeRMEED-3, Figures 2e and 2f). The clockwise rotation of the anticyclonic eddies led to intensified northward flow along the steep slope offshore of the Bahamas (Figures 3 and 4). Contrary to expectations, we observed no along-slope southward flow during the cyclonic eddy (Figure 5). The levels of turbulent dissipation measured during the anticyclonic eddies were also much larger than those observed during the cyclonic eddy (Figures 3–5). In particular, we documented a range of dissipative processes, reflecting a complex interaction between the eddy flow and the steep and rough topographic slope (Section 4). The contrast between dissipation levels associated with anticyclonic and cyclonic eddies agrees with the conclusions of Clément et al. (2016), who found enhanced high-frequency internal wave activity during anticyclonic eddies. Note, though, that high-resolution images of SST (Figure 2f) and our vessel-mounted ADCP survey (Figure 5) suggest that the cyclonic eddy observed during MeRMEED-3 was smaller and/or not as close to the slope as it appeared in SLA (Figure 2e).

We can appraise the longer-term representativeness of our cruise-based diagnostics by accessing the flow variability measured by the mooring WB1 (Figure 20) between December 2015 and March 2017. In general, during periods when no eddy is present, flow is northward in the upper 1,000 m ($v < 0.5$ ms^{-1} in the

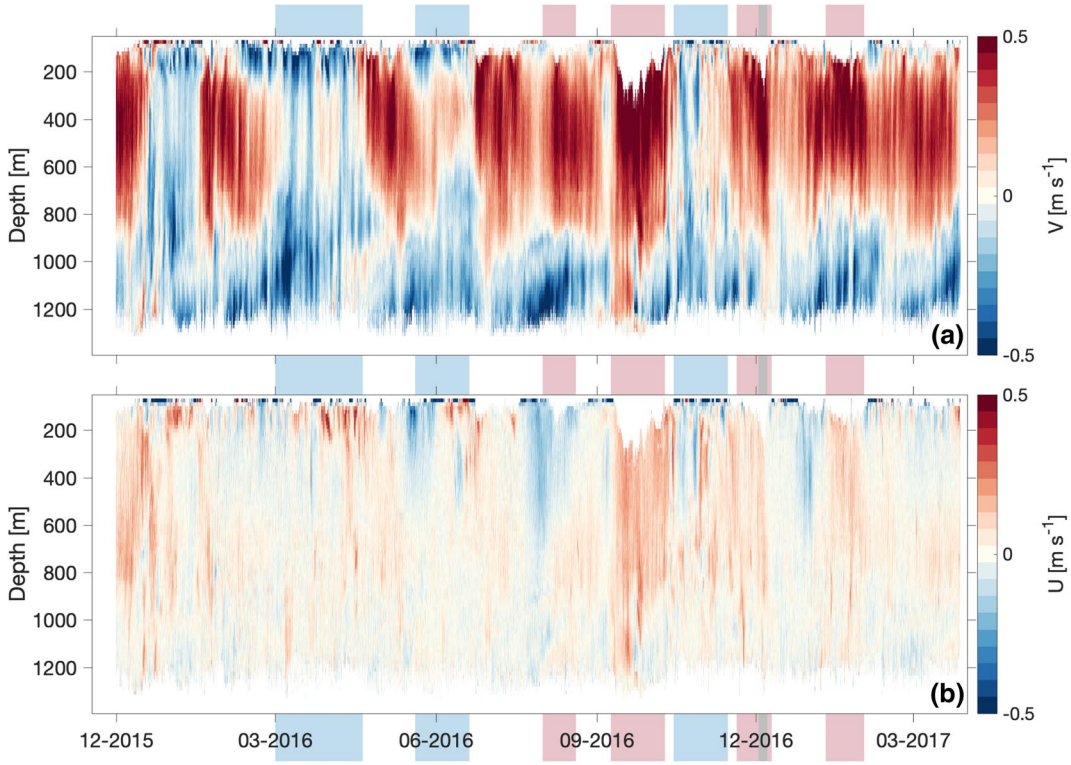

Figure 20. (a) Meridional and (b) zonal velocity from the WB1 mooring shown by the white circle in Figure 1. The blue bars mark cyclonic eddies and the red bars anticyclonic eddies. The gray bar indicates the duration of MeRMEED-1. Units: m s^{-1}. Date format: MM-YYYY. MeRMEED, Mechanisms Responsible for Mesoscale Eddy Energy Dissipation.

upper 1,000 m). During anticyclonic eddies, the flow at WB1 is northward in the upper 1,000 m with $v >$ 0.5 ms^{-1}. In contrast, the magnitude of the flow at WB1 during cyclonic eddies is weaker ($<$ 0.2 ms^{-1}), and its direction can be either northward or southward. This contrast between anticyclonic and cyclonic eddies is consistent with the observations in Clément et al. (2016), and demonstrates that the along-slope flow observed during MeRMEED-1 and MeRMEED-2 is similar to that linked to other anticyclones sampled by the mooring. These results suggest that, in the absence of an eddy, the flow along the slope offshore of the Bahamas at 26.5°N is northward. The northward flow associated with an anticyclonic eddy reinforces this background flow, predictably triggering the turbulent processes that we sampled during MeRMEED-1 and MeRMEED-2. However, the southward flow of cyclonic eddies opposes the background northward flow, leading to weak along-slope flow and reduced turbulent dissipation (Clément et al., 2016).

To place the MeRMEED study, and the processes identified therein, in a global context, we consider how the topography and eddy activity in our study area compare to conditions in other western boundary regions. In the MeRMEED area, topography is particularly steep where the Bahamian islands rise abruptly out of the abyssal Atlantic (with topographic slopes as high as 3:4). Such topography is not uncommon in other western boundaries. For example, there is similarly steep topography throughout the other islands of the Lucayan Archipelago and the Lesser Antilles. Beyond the North Atlantic, the topography of the island chains of the western Pacific is similarly steep, and has been the focus of other investigations of flow-topography interactions (MacKinnon et al., 2019; Zeiden et al., 2019). Flow-topography interactions have also been explored in the context of a deep western boundary current flowing along the steep slopes of the Orkney Passage (A. C. Naveira Garabato et al., 2019). The eddy activity in the MeRMEED study area is typical of mid-latitude regions in the global ocean (Chelton et al., 2011), which are characterized by relatively high concentrations of incident eddies. Further, the MeRMEED study area and, more widely, the western mid-Atlantic, is a region of elevated density of eddy terminations, with up to 4 eddy terminations per 1° square (Chelton et al., 2011). Compared to other western boundary regions in the global ocean, the

MeRMEED study area is a typical eddy sink, with mesoscale eddy energy loss in this region of between 0.005 Wm^{-2} and 0.010 Wm^{-2} (Zhai et al., 2010). On the basis of these comparisons, we may thus expect the eddy-topography interactions described within the MeRMEED study area to be relevant to other western boundary regions of the global ocean.

6. Summary and Conclusions

This study investigates the rates and mechanisms by which mesoscale eddies dissipate and decay upon interacting with a western boundary. We used targeted ship-based observations of microstructure and flow velocity, satellite altimetry, and a mooring record, to identify several important processes inducing elevated turbulent dissipation as eddies impinge on the steep and rough topography of the western boundary. We completed three short-duration (7–11 days) cruises, and sampled two anticyclonic eddies and one cyclonic eddy. Our sampling focused on a protruding escarpment offshore of Great Abaco, Bahamas, where the clockwise (anticlockwise) rotation of an anticyclonic (cyclonic) eddy implies northward (southward) flow along the slope. During these cruises, we identified a "zoo" of dissipative processes that contribute to the decay of the observed eddies in our study area. These processes reflect direct flow-topography interactions between the eddies' balanced flow and the topography of the protruding escarpment. We also document nonlocal effects associated with how the topography imprints on the downstream structure of the flow.

During both anticyclonic eddies, the eddy flow separates from the topography downstream of the escarpment, forming a slanted shear layer that mimics the slope of the escarpment. Here, we observed elevated dissipation in the region of cyclonic shear, where the Richardson number is low. However, the highest dissipation rates were measured in a layered segment of the flow, where a change in the sign of the isopycnal gradient of PV indicated conditions favorable to the development of horizontal shear instability. Just south (upstream) of the escarpment, we observed a recirculation of the northward eddy flow due to topographic blocking. Here, flow steers to the west, leading to southward flow adjacent to the slope and the generation of negative PV, with conditions favorable for centrifugal instability (e.g., Gula et al., 2016) that can be linked to the observed elevated turbulence. Where the northward flow of the anticyclonic eddies shoots over the escarpment, we documented $\mathcal{O}(1)$ Froude number, enhanced dissipation and internal wave generation, indicative of hydraulic control (Dossmann et al., 2016). Finally, in northward flow within 1–2 km of the slope, we consistently measured elevated dissipation, high Rossby number, and variable PV associated with small-scale flow recirculations. These signatures are potentially consistent with a range of candidate processes that are not well constrained by our observations.

Theoretical and modeling studies identify numerous mechanisms for the direct cascade of energy from the mesoscale to small-scales, where energy dissipates. These studies often rely on simplified representations of eddies, flow and topography, and are valuable for identifying the relevant instabilities for a given flow-topography configuration. Here, we show that the impingement of eddies on the complex topography of the western boundary offshore of the Bahamas does not favor a specific mechanism of eddy decay. Instead, we observe a broad range of flow-topography interaction processes, some of which echo, and some of which are distinct from, processes highlighted by existing theoretical and numerical studies.

The dissipative processes documented by MeRMEED are specific to the topographic configuration in this sector of the Atlantic Ocean's western boundary. The topographic slope offshore of Great Abaco is steep and rough, and most of the interactions we identified in this area relied on topographic roughness protruding into the eddy flow in the upper 1,000 m. Such topography is, however, common along island chains that span much of the western boundaries in the Pacific and Atlantic oceans. Thus, we conjecture that the interactions documented in this work may be common. A quantitative extrapolation of the relative importance of the dissipative processes discussed here to the global ocean is beyond the scope of this study, and will be the subject of future work. While contributions from processes other than eddy interactions with topography cannot be discounted, tidal energy conversion in the area is modest and there is no apparent relationship of measured dissipation patterns to wind forcing.

Zhai et al. (2010) showed that ocean western boundaries are prominent sinks of eddy energy, but the direction of the cascade of energy from the mesoscale was not clear in their altimetry-based framework. The analysis presented here reveals dynamics governing the decay of mesoscale eddies at a western boundary,

via a direct cascade of energy culminating in the generation of small-scale turbulence. This turbulence is linked to a "zoo" of processes triggered by flow-topography interactions. Our results highlight the complexity of the eddy energy pathways to dissipation at western boundaries, and provide a mechanism-discerning point of reference for the realistic representation of eddy dissipation in ocean models. In a follow-up paper, we will quantify the relative contributions of the processes documented here to the dissipation of eddies within the MeRMEED study area.

Data Availability Statement

The VMP, vessel-mounted ADCP, CTD and mooring data are available from the British Oceanography Data Centre and can be accessed via the following DOIs: Moored ADCP: https://doi.org/10/fjpx, MeRMEED-1: https://doi.org/10/fjp7, MeRMEED-2: https://doi.org/10/fjqh, MeRMEED-3: https://doi.org/10/fjq2. SLA data can be accessed through http://marine.copernicus.eu/. GHRSST MUR SST data can be accessed at https://www.ghrsst.org/. Multibeam-based bathymetry data is available at https://www.ncei.noaa.gov/.

Acknowledgments
The authors would like to thank the crew, captain, and marine operations team of the *R/V F. G. Walton Smith* for their support and assistance during the three MeRMEED cruises. We are extremely grateful to the National Marine Facilities team at the National Oceanography Centre, Southampton, whose efforts made this work possible, as well as the science team and crew responsible for the RAPID mooring deployments (http://www.rapid.ac.uk). Andy Hogg provided helpful comments through various discussions on earlier versions of this analysis. The authors would also like to thank two anonymous reviewers for their helpful and constructive comments. The MeRMEED project, DGE, EFW, ACNG and AF were funded under Natural Environment Research Council standard grant NE/N001745/2. ACNG further acknowledges the support of the Royal Society and the Wolfson Foundation.

References

Brink, K. H., & Lentz, S. J. (2009). Buoyancy arrest and bottom Ekman transport. Part I: Steady flow. *Journal of Physical Oceanography*, *40*(4), 621–635. https://doi.org/10.1175/2009JPO4266.1

Chelton, D. B., Schlax, M. G., & Samelson, R. M. (2011). Global observations of nonlinear mesoscale eddies. *Progress in Oceanography*, *91*(2), 167–216. https://doi.org/10.1016/j.pocean.2011.01.002

Cherian, D. A., & Brink, K. H. (2016). Offshore transport of shelf water by deep-ocean eddies. *Journal of Physical Oceanography*, *46*(12), 3599–3621. https://doi.org/10.1175/JPO-D-16-0085.1

Cherian, D. A., & Brink, K. H. (2018). Shelf flows forced by deep-ocean anticyclonic eddies at the shelf break. *Journal of Physical Oceanography*, *48*(5), 1117–1138. https://doi.org/10.1175/JPO-D-17-0237.1

Clément, L., Frajka-Williams, E., Sheen, K. L., Brearley, J. A., & Garabato, A. C. N. (2016). Generation of internal waves by eddies impinging on the western boundary of the North Atlantic. *Journal of Physical Oceanography*, *46*(4), 1067–1079. https://doi.org/10.1175/JPO-D-14-0241.1

Dewar, W. K., Berloff, P., & Hogg, A. M. (2011). Submesoscale generation by boundaries. *Journal of Marine Research*, *69*(4–5), 501–522.

Dewar, W. K., & Hogg, A. M. (2010). Topographic inviscid dissipation of balanced flow. *Ocean Modelling*, *32*(1), 1–13. https://doi.org/10.1016/j.ocemod.2009.03.007

Dossmann, Y., Rosevear, M. G., Griffiths, R. W., Hogg, A. McC., Hughes, G. O., & Copeland, M. (2016). Experiments with mixing in stratified flow over a topographic ridge. *Journal of Geophysical Research: Oceans*, *121*(9), 6961–6977. https://doi.org/10.1002/2016JC011990

Fernández-Castro, B., Evans, D. G., Frajka-Williams, E., Vic, C., & Naveira-Garabato, A. C. (2020). Breaking of internal waves and turbulent dissipation in an anticyclonic mode Water Eddy. *Journal of Physical Oceanography*, *50*(7), 1893–1914. https://doi.org/10.1175/JPO-D-19-0168.1

Ferrari, R., & Wunsch, C. (2009). Ocean circulation kinetic energy: Reservoirs, sources and sinks. *Annual Reviews of Fluid Mechanics*, *41*, 253–282. https://doi.org/10.1146/annurev.fluid.40.111406.102139

Girton, J. B., Pratt, L. J., Sutherland, D. A., & Price, J. F. (2006). Is the Faroe Bank Channel overflow hydraulically controlled? *Journal of Physical Oceanography*, *36*(12), 2340–2349. https://doi.org/10.1175/JPO2969.1

Gula, J., Molemaker, M. J., & McWilliams, J. C. (2015), Topographic vorticity generation, submesoscale instability and vortex street formation in the Gulf Stream, *Geophysical Research Letters*, *42*(10), 4054–4062, https://doi.org/10.1002/2015GL063731

Gula, J., Molemaker, M. J., & McWilliams, J. C. (2016). Topographic generation of submesoscale centrifugal instability and energy dissipation. *Nature Communications*, *7*(12), 811.

Hogg, A. M., Dewar, W. K., Berloff, P., & Ward, M. L. (2011). Kelvin wave hydraulic control induced by interactions between vortices and topography. *Journal of Fluid Mechanics*, *687*, 194–208. https://doi.org/10.1017/jfm.2011.344

Hoskins, B. J. (1974). The role of potential vorticity in symmetric stability and instability. *Quarterly Journal of the Royal Meteorological Society*, *100*(425), 480–482. https://doi.org/10.1002/qj.49710042520

IOC, SCOR, and IAPSO. (2010). *The international thermodynamic equation of seawater - 2010: Calculation and use of thermodynamic properties*. Intergovernmental Oceanographic Commission, Manuals and Guides No. 56, UNESCO (English), p. 196.

Johns, W. E., Beal, L. M., Baringer, M. O., Molina, J. R., Cunningham, S. A., Kanzow, T., et al. (2008). Variability of shallow and deep western boundary currents off the Bahamas during 2004-05: Results from the 26N RAPID-MOC Array. *Journal of Physical Oceanography*, *28*, 605–623.

Klymak, J. M., & Gregg, M. C. (2004). Tidally generated turbulence over the Knight Inlet sill. *Journal of Physical Oceanography*, *34*(5), 1135–1151. https://doi.org/10.1175/1520-0485(2004)034<1135:TGTOTK>2.0CO;2

Klymak, J. M., Legg, S. M., & Pinkel, R. (2010), High-mode stationary waves in stratified flow over large obstacles, *Journal of Fluid Mechanics*, *644*, 321–336, https://doi.org/10.1017/S0022112009992503

MacCready, P., & Pawlak, G. (2001). Stratified flow along a corrugated slope: Separation drag and wave drag. *Journal of Physical Oceanography*, *31*(10), 2824–2839. https://doi.org/10.1175/1520-0485(2001)031<2824:SFAACS>2.0.CO;

MacKinnon, J. A., Alford, M. H., Voet, G., Zeiden, K. L., Shaun Johnston, T. M., Siegelman, M., et al. (2019). Eddy wake generation from broadband currents near Palau. *Journal of Geophysical Research: Oceans*, *124*(7), 4891–4903. https://doi.org/10.1029/2019JC014945

MacKinnon, J. A., Zhao, Z., Whalen, C. B., Waterhouse, A. F., Trossman, D. S., Sun, O. M., et al. (2017). Climate process team on internal wave-driven ocean mixing. *Bulletin of the American Meteorological Society*, *98*(11), 2429–2454. https://doi.org/10.1175/BAMS-D-16-0030.1

McCarthy, G. D., Smeed, D. A., Johns, W. E., Frajka-Williams, E., Moat, B. I., Rayner, D., et al. (2015). Measuring the Atlantic meridional overturning circulation at 26Â°N. *Progress in Oceanography*, *130*, 91–111. https://doi.org/10.1016/j.pocean.2014.10.006

McWilliams, J. C., Molemaker, M. J., & Yavneh, I. (2004). Ageostrophic, anticyclonic instability of a geostrophic, barotropic boundary current. *Physics of Fluids*, *16*(10), 3720–3725. https://doi.org/10.1063/1.1785132

Naveira Garabato, A. (2009). RRS James Cook Cruise 29, 01 Nov-22 Dec 2008: SOFine cruise report; Southern Ocean Finestructure. *National Oceanography Centre Southampton Cruise Report*, *35*, 216.

Naveira Garabato, A. C., Frajka-Williams, E. E., Spingys, C. P., Legg, S., Polzin, K. L., Forryan, A., et al. (2019). Rapid mixing and exchange of deep-ocean waters in an abyssal boundary current. *Proceedings of the National Academy of Sciences*, *116*(27), 13233–13238. https://doi.org/10.1073/pnas.1904087116

Nikurashin, M., & R. Ferrari (2011), Global energy conversion rate from geostrophic flows into internal lee waves in the deep ocean. *Geophysical Research Letters*, *38*(8), L08610. https://doi.org/10.1029/2011GL046576

Oakey, N. S. (1982). Determination of the rate of dissipation of turbulent energy from simultaneous temperature and velocity shear microstructure measurements. *Journal of Physical Oceanography*, *12*(3), 256–271. https://doi.org/10.1175/1520-0485(1982)012<0256:DOTROD>2.0.CO;2

Scott, R. B., Goff, J. A., Naveira Garabato, A. C., & Nurser, A. J. G. (2011). Global rate and spectral characteristics of internal gravity wave generation by geostrophic flow over topography. *Journal of Geophysical Research*, *116*(C9), C09029. https://doi.org/10.1029/2011JC007005

Scott, R. B., & Wang, F. (2005). Direct evidence of an oceanic inverse kinetic energy cascade from satellite altimetry. *Journal of Physical Oceanography*, *35*, 1650–1666.

Sheen, K. L., Brearley, J. A., Naveira Garabato, A. C., Smeed, D. A., Waterman, S., Ledwell, J. R., et al. (2013). Rates and mechanisms of turbulent dissipation and mixing in the Southern Ocean: Results from the Diapycnal and Isopycnal Mixing Experiment in the Southern Ocean (DIMES). *Journal of Geophysical Research: Oceans*, *118*(6), 2774–2792. https://doi.org/10.1002/jgrc.20217

St Laurent, L. C., & Thurnherr, A. M. (2007). Intense mixing of lower thermocline water on the crest of the Mid-Atlantic Ridge. *Nature*, *448*, 680.

Thompson, A. F., Lazar, A., Buckingham, C., Naveira Garabato, A. C., Damerell, G. M., & Heywood, K. J. (2016). Open-ocean submesoscale motions: A full seasonal cycle of mixed layer instabilities from gliders. *Journal of Physical Oceanography*, *46*(4), 1285–1307. https://doi.org/10.1175/JPO-D-15-0170.1

Trowbridge, J. H., & Lentz, S. J. (1991). Asymmetric behavior of an oceanic boundary layer above a sloping bottom. *Journal of Physical Oceanography*, *21*(8), 1171–1185. https://doi.org/10.1175/1520-0485(1991)021<1171ABOAOB>2.0.CO;2

Vallis, G. K. (2017). *Atmospheric and oceanic fluid dynamics: Fundamentals and large-scale circulation* (2nd ed.). Cambridge, UK: Cambridge University Press. https://doi.org/10.1017/9781107588417

Vic, C., Naveira Garabato, A. C., Green, J. A. M., Waterhouse, A. F., Zhao, Z., Melet, A., et al. (2019). Deep-ocean mixing driven by small-scale internal tides. *Nature Communications*, *10*(1), 2099. https://doi.org/10.1038/s41467-019-10149-5

Warner, S. J., & MacCready, P. (2009). Dissecting the pressure field in tidal flow past a headland: When is form drag "Real"? *Journal of Physical Oceanography*, *39*(11), 2971–2984. https://doi.org/10.1175/2009JPO4173.1

Warner, S. J., & MacCready, P. (2014). The dynamics of pressure and form drag on a sloping headland: Internal waves versus eddies. *Journal of Geophysical Research: Oceans*, *119*(3), 1554–1571. https://doi.org/10.1002/2013JC009757

Wunsch, C. (1997). The vertical partition of oceanic horizontal kinetic energy. *Journal of Physical Oceanography*, *27*(8), 1770–1794. https://doi.org/10.1175/1520-0485(1997)027<1770:TVPOOH>2.0.CO;2

Zeiden, K. L., Rudnick, D. L., & MacKinnon, J. A. (2019). Glider observations of a mesoscale oceanic island wake. *Journal of Physical Oceanography*, *49*(9), 2217–2235. https://doi.org/10.1175/JPO-D-18-0233.1

Zhai, X., Johnson, H. L., & Marshall, D. P. (2010). Significant sink of ocean-eddy energy near western boundaries. *Nature Geoscience*, *3*, 608.

Zhang, W. G., & Gawarkiewicz, G. G. (2015). Dynamics of the direct intrusion of Gulf Stream ring water onto the Mid-Atlantic Bight shelf. *Geophysical Research Letters*, *42*(18), 7687–7695. https://doi.org/10.1002/2015GL065530

Zhang, W. G., & Partida, J. (2018). Frontal subduction of the Mid-Atlantic Bight shelf water at the onshore edge of a warm-core ring. *Journal of Geophysical Research: Oceans*, *123*(11), 7795–7818. https://doi.org/10.1029/2018JC013794